Integrability Breaking in Periodically Driven Systems

Hunter Brodie

Wadham College

University of Oxford

A thesis submitted for the degree of

MSc in Mathematical and Theoretical Physics

Trinity 2026

Acknowledgements

I would like to thank Professor Fabian Essler and Dr. Sascha Gehrmann for their guidance throughout this project. I am grateful to my parents for their support and encouragement throughout this year.

Abstract

This project studies the effects of a single non-integrable impurity in an otherwise integrable one-dimensional Floquet XXZ quantum circuit. Integrable systems possess an extensive number of conserved quantities that constrain dynamics and inhibit thermalization. By introducing a single local impurity that breaks the Yang-Baxter structure, we study how these conserved quantities decay and how thermalization emerges at late times.

Using GPU-accelerated numerical simulations, the dynamics of systems of up to 30 spins were studied for a variety of initial states and observables. Several complementary diagnostics were used to characterize thermalization dynamics, including early-time exponential decay fits, time-averaged expectation values, and plateau-entry times. The early-time dynamics exhibited approximately exponential relaxation with decay times that often scaled linearly with system size, while plateau-entry times suggested a slower, approximately quadratic scaling. This indicates that different diagnostics probe distinct dynamical regimes.

Overall, this work highlights both the fragility of integrability in Floquet quantum circuits and the complexity of thermalization dynamics.

Contents

List of Figures

Introduction

Floquet systems are quantum systems governed by time-periodic Hamiltonians satisfying $H(t) = H(t+T)$ for some period T [5, 11, 37]. Since the Hamiltonian is time-dependent, Floquet systems do not generally conserve energy and are therefore expected to thermalize toward infinite-temperature states [1, 5, 10]. As a result, Floquet quantum circuits provide a natural framework for studying nonequilibrium quantum dynamics and thermalization.

A particularly important exception occurs in integrable Floquet systems. These systems have an extensive family of conserved quantities that constrain the dynamics and prevent conventional thermalization [2, 13, 23]. Instead of heating to infinite-temperature, integrable Floquet systems may relax toward nonthermal steady states, if they relax at all [13,35]. Since integrability is highly fragile, even small perturbations can break integrability and change the long-time dynamics of the system [10, 26].

This thesis studies the breakdown of integrability in a one-dimensional Floquet XXZ quantum circuit induced by a single local non-integrable impurity. Although this impurity acts only locally, it is enough to break integrability in the system. The primary goal of this work is to investigate how the resulting thermalization time scales with system size and how different diagnostics probe distinct relaxation regimes.

The numerical simulations are performed through exact calculation using GPU-accelerated CUDA implementations [29,30]. By exploiting the locality and brickwork structure of the XXZ Floquet circuit, systems of up to 30 spins can be simulated on consumer-grade laptops.

The first chapter reviews the essential background information on Floquet systems and brickwork Floquet circuits. The second chapter introduces integrability, the Eigenstate Thermalization Hypothesis, and the XXZ Floquet model studied in this thesis. The third chapter details the numerical methods and GPU implementation used for the simulations. The fourth presents the numerical results, and the final chapter discusses possible directions for future work.

The CUDA source code used to generate the simulations is available upon request.

Chapter 1

Floquet Systems

1.1 Floquet Unitary

Periodically driven systems are characterized by a Hamiltonian that for some fixed period T is periodic in time, or $H(t) = H(t+T)$ [5, 11, 37]. We can obtain the time evolution operator for a constant Hamiltonian from the unitary time evolution operator defined in Eq. 1.1. For a time-dependent Hamiltonian, the evolution operator is given by the time-ordered exponential in Eq. 1.2.

$$U(t) = e^{-iHt/\hbar} \tag{1.1}$$

$$U(t) = \mathcal{T} e^{-\frac{i}{\hbar}\int_0^t H(t')dt'} \tag{1.2}$$

The time-ordering operator $\mathcal{T}$ is required since the Hamiltonian at different times does not generally commute [11, 37]. For Floquet systems, the Hamiltonian is time-periodic, so the time evolution operator for a period T can be obtained using Eq. 1.2. The Floquet unitary is therefore defined as

$$U_F = U(T) = \mathcal{T} e^{-\frac{i}{\hbar}\int_0^T H(t')dt'} \tag{1.3}$$

for a Hamiltonian with period T [37]. The system can then be evolved in discrete time increments by raising the Floquet unitary to an integer power. The stroboscopic evolution of the unitary at integer multiples of the period is

$$U(nT) = U_F^n \tag{1.4}$$

Therefore, the Floquet unitary is useful in determining the long term behavior of a periodically driven system at discrete times [5,11]. Since the Hamiltonian is explicitly time-dependent, energy is not generally conserved, and generic interacting Floquet systems are expected to absorb energy and thermalize toward infinite-temperature states [1,5,24,33].

Since U_F is guaranteed to be unitary, it is always possible to rewrite the Floquet unitary as

$$U_F = e^{-iH_F T} \tag{1.5}$$

where H_F is Hermitian, and is also referred to as the Floquet Hamiltonian [5,37]. Throughout this thesis, natural units with $\hbar = 1$ are used. The Floquet Hamiltonian can be useful for analyzing some of the properties for the system. The structure of the Floquet Hamiltonian can also provide insight into the integrability of the system.

1.2 Brickwork Floquet Circuits

In this thesis, the one-dimensional brickwork Floquet circuit is studied. These provide a simple framework for studying thermalization and integrability breaking [7,17].

1.2.1 Brickwork Structure

Floquet quantum circuits are usually represented by a series of unitary operators sequentially acting on the system. These unitary operators are analogous to the quantum gates [28], and usually act on one or two spins at a time. In many-body settings, the spins are typically defined on a lattice. The circuits studied in this thesis have periodic boundary conditions. One of the most common structures of Floquet circuits, and the one that is studied here, is the brickwork circuit [17].

In the brickwork, there are two layers of staggered nearest neighbor two spin unitaries that form the Floquet unitary itself. Layers can be repeatedly added to evolve the system in time, giving rise to the brickwork structure [17]. Fig. 1.1 shows the brickwork pattern, where the nearest neighbor unitaries are the boxes, and the arrows represent the lattice spins as time increases vertically.

The brickwork circuit can be interpreted as a periodically driven system generated by two staggered constant Hamiltonians acting sequentially for time $T/2$ [5]. The Floquet unitary can then be written as $U_F = U_2 U_1$, where U_1 is the time evolution

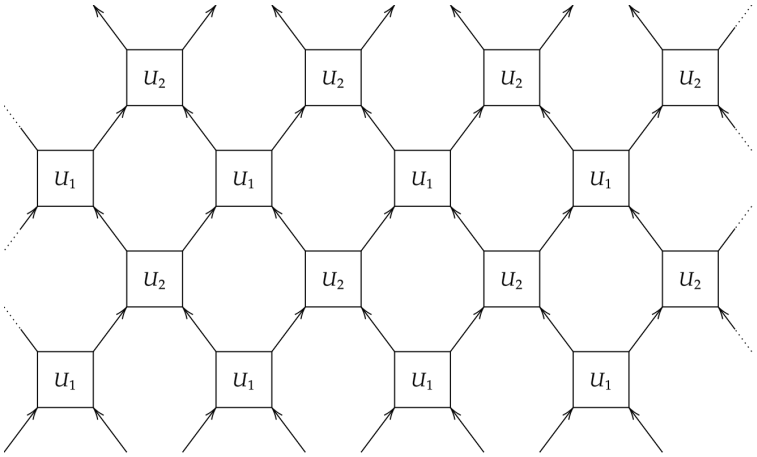

Figure 1.1: Time Evolution of a 1D Floquet Circuit

operator on the Hamiltonian governing the first layer, and U_2 is the time evolution operator on the Hamiltonian governing the second layer [17]. Since the nearest neighbor gates are staggered, it is important to note that all gates in the first layer commute with each other, and the same is true for the second layer. This structure enables efficient classical computation of the circuit.

1.2.2 Locality

One very important feature of the brickwork circuit is locality [6, 25]. In many-body systems, locality means that each body only interacts with other bodies that are close by. In other words, any information in the system must travel at a finite speed throughout the system [25]. To have a local Hamiltonian, the Hamiltonian must be able to be written as a sum of terms, with each term acting on a non-extensive subset of the system. This requirement is fulfilled in the brickwork circuit since it is only made up of nearest neighbor terms [17]. Therefore, the information in the brickwork circuit travels outward in a light cone that can only advance one site per period [6,25].

One important aspect of locality is the appearance of well-defined subsystems. It allows us to define useful concepts such as entanglement entropy and local observables such that they only depend weakly on distant parts of the system [12,25]. The locality of the brickwork circuit plays a central role in the thermalization dynamics studied in this thesis, since the effects of the local impurity can only propagate through the system at a finite velocity.

Chapter 2

Integrability and the Eigenstate Thermalization Hypothesis

2.1 Integrability

Integrability plays a central role in quantum many-body systems [2, 13, 23]. Generic, non-integrable many-body systems are expected to evolve according to the Eigenstate Thermalization Hypothesis, which leads to complete thermalization regardless of the starting conditions [9, 34, 38]. Integrable systems are constrained by the conserved quantities that exist, such that they fail to thermalize to a conventional thermal ensemble [13, 35]. For systems governed by time-independent Hamiltonians, they are considered integrable if there exists an extensive set of independent conserved operators Q_i, such that each Q_i commutes with the Hamiltonian [13, 23]. Each operator must be either local or quasi-local. Quasi-local operators are similar to like local operators, but can act on all sites as long as the operator strength decays rapidly with distance [20].

Integrability is an important property of many-body systems, since integrable systems are able to be solved exactly, allowing them to be studied analytically. Phenomena such as elastic scattering are often most clearly understood in integrable regimes [2, 23]. Integrable Floquet systems are particularly important because they can prevent the generic infinite heating due to the conserved quantities involved [1, 5]. Integrability is very fragile; small imperfections in the circuit that break integrability can lead to drastic changes in behavior, as the algebraic structure underlying the conserved quantities is easily destabilized [10, 13]. The contrast between integrable and non-integrable dynamics provides a natural framework for studying thermalization.

For Floquet systems, the fundamental object that governs the system is not a Hamiltonian, but the Floquet unitary U_F [5]. The same general principles apply to Floquet systems, except that the conserved operators need to commute with the Floquet unitary rather than the Hamiltonian. When the Floquet system is integrable, the system is severely constrained by the conserved quantities, as in the time-independent Hamiltonian case, and does not heat to infinite-temperature. This sharply contrasts with a non-integrable Floquet system, as those systems do not generally conserve energy.

2.1.1 Conserved Quantities

Systems are considered integrable when they have an extensive number of operators independent of the time evolution operator that commute with the time evolution operator [13, 23]. This naturally leads to a number of extensive conserved quantities of the system that are associated with those local operators. This can be seen easily by applying the observable to the state at discrete time n

$$\langle\psi\left|\left(U_F^{-1}\right)^n O U_F^n\right|\psi\rangle = \langle\psi\left|O\left(U_F^{-1}\right)^n U_F^n\right|\psi\rangle = \langle\psi|O|\psi\rangle \tag{2.1}$$

We can see that the expectation value of the observable must be conserved throughout the time evolution. It follows that the expectation value of the observable cannot relax to the infinite-temperature value [13,35]. This is what allows us to use local observables as a diagnostic for when the system thermalizes, as these formerly conserved local operators must decay to a very small plateau value.

2.2 Eigenstate Thermalization Hypothesis

The Eigenstate Thermalization Hypothesis (ETH) proposes an explanation for why isolated quantum systems exhibit thermal behavior, even though their time evolution is governed by reversible dynamics [9, 10, 38]. Unlike classical systems, an isolated quantum system evolves unitarily, so it can never become a thermal mixed state. ETH asserts that for non-integrable quantum systems, the individual eigenstates themselves encode the thermal expectation values [9, 10, 38]. That is, if you take a single energy eigenstate and measure an observable, the expectation value of that observable will match what you expect for the appropriate thermal ensemble.

ETH states that the diagonal matrix elements of local observables in the energy basis will vary smoothly as a function of energy, while the off-diagonal elements are exponentially suppressed in system size and behave effectively as random variables [10,38]. This behavior has been tested numerically in finite many-body systems, where ETH is diagnosed by diagonalizing local observables in the energy eigenbasis and examining the smoothness of diagonal elements and the suppression of off-diagonal ones [22]. As a result, generic non-integrable quantum systems relax toward thermal expectation values and exhibit small fluctuations around the equilibrium [10, 34].

Specifically, elements of the local observables in the energy eigenbasis take the form [38]

$$\bar{E} = \frac{E_n + E_m}{2}, \quad \omega = E_n - E_m \tag{2.2}$$

$$O_{nm} = \delta_{n,m} g_O(\bar{E}) + (1 - \delta_{n,m}) \exp[-S(\bar{E})/2] f_O(\bar{E}, \omega) R_{nm} \tag{2.3}$$

where g_O is a smooth function, R_{nm} are random variables with zero mean and unit variance, and f_O is a smooth function related to linear response theory [10, 38].

At infinite temperature, quantum many-body systems are described by the maximally mixed state. In the canonical ensemble, the density matrix is

$$\rho = \frac{1}{Z} e^{-\beta H} \tag{2.4}$$

where $\beta = 1/T$, H is the Hamiltonian of the system, and Z is the partition function. In the infinite temperature limit $\beta \to 0$, the Boltzmann weight is independent of energy and the density matrix is reduced to

$$\rho_\infty = \frac{\mathrm{id}}{D} \tag{2.5}$$

where D is the dimension of the Hilbert space. In this limit, every configuration is equally likely [12].

The expectation of a local observable in the infinite temperature limit is therefore its normalized trace,

$$\langle O \rangle = \mathrm{Tr}\left[O \rho_\infty\right] = \frac{1}{D} \mathrm{Tr}[O] \tag{2.6}$$

This makes local observables, like the $Z_i Z_j$ observables, natural diagnostics for when the system thermalizes. Since we are studying small systems of up to 30 spins,

the thermalized values of the local observables will fluctuate around the near-zero values for traceless observables. In generic non-integrable Floquet systems, ETH is expected to govern the late-time dynamics, leading to thermalization toward an effective infinite-temperature state [5, 10].

2.3 The XXZ Model

The Heisenberg XXZ model is a widely studied integrable model [2,23]. It differs from the simpler XXX model by introducing an anisotropy parameter into the Hamiltonian. The Hamiltonian of the XXZ model is

$$H_{XXZ} = -T \sum_{j=1}^{N} \left(\sigma_j^x \sigma_{j+1}^x + \sigma_j^y \sigma_{j+1}^y + \Delta \sigma_j^z \sigma_{j+1}^z \right) \tag{2.7}$$

To define the Floquet unitary, we consider the time evolution generated by staggered nearest-neighbor XXZ terms [17]. We can define a two-site XXZ Hamiltonian as

$$H_{XXZ}^{(j)} = -T \left(\sigma_j^x \sigma_{j+1}^x + \sigma_j^y \sigma_{j+1}^y + \Delta \sigma_j^z \sigma_{j+1}^z \right) \tag{2.8}$$

where the Hamiltonian acts on spins j and $j+1$. The Floquet unitary can then be written as

$$U_F = \exp \left[\sum_{j \text{ even}}^{L} -iH_{XXZ}^{(j)} \right] \exp \left[\sum_{j \text{ odd}}^{L} -iH_{XXZ}^{(j)} \right] \tag{2.9}$$

In each of the staggered sums in the exponentials, all the terms commute with each other since they act on independent pairs of spins. This is important to note, as the commuting structure allows for each exponential to factorize into products of two-site unitaries [17]. Therefore, the Floquet unitary can be rewritten as

$$U_F = \left(\prod_{j \text{ even}} e^{-iH_{XXZ}^{(j)}} \right) \left(\prod_{j \text{ odd}} e^{-iH_{XXZ}^{(j)}} \right) \tag{2.10}$$

This is important for numerically simulating the circuit, since the dynamics can be implemented through local bitwise operations on two-spin subsystems rather than constructing the full Floquet unitary [28]. Within each layer, the local gates commute since they act on disjoint pairs of spins, although the two staggered layers do not generally commute with each other.

2.3.1 Integrability of the XXZ Model

The XXZ model is integrable because it admits a family of commuting transfer matrices [2, 14, 23].

$$[\mathbb{T}(u), \mathbb{T}(v)] = 0, \, \forall u, v \in \mathbb{C} \tag{2.11}$$

parameterized by the spectral parameter u. Expanding the logarithm of the transfer matrix in the spectral parameter gives an extensive set of mutually commuting conserved quantities [14, 23]. We now introduce the R matrix for our XXZ Hamiltonian, along with the transfer matrix built from the R matrices.

$$R_{j,k}(u) = \begin{bmatrix} \sinh(u+\eta) & 0 & 0 & 0 \\ 0 & \sinh(u) & \sinh\eta & 0 \\ 0 & \sinh(\eta) & \sinh u & 0 \\ 0 & 0 & 0 & \sinh(u+\eta) \end{bmatrix} \tag{2.12}$$

$$\mathbb{T}(u) = \mathrm{Tr}_a \left[R_{a1}(u) R_{a2}(u) \cdots R_{aN}(u) \right] \tag{2.13}$$

where the R-matrix $R_{j,k}$ acts on the j^{th} and k^{th} spins. We introduce an auxiliary spin a to construct the transfer matrix. The transfer matrix can be represented graphically as a sequence of R-matrices connected through an auxiliary space with periodic boundary conditions [14, 19]. Using this notation, the commutation relation between transfer matrices can be understood through the Yang-Baxter equation [2, 14, 19]. Graphically, the Yang-Baxter equation allows a swap operator carrying spectral parameter $u - v$ to be moved through the transfer-matrix network. This is seen in Fig. 2.1, where the boxes are matrices with a parameterization, and the circles are the inverses. Therefore, a swap operator and its inverse can be inserted into the diagram.

Repeated application of the Yang-Baxter equation allows the swap operator to be moved through the transfer matrix network, thereby proving the transfer-matrix commutation relation [14, 19]. The conserved quantities can then be generated from the derivatives of the logarithm of the transfer matrix,

$$Q_n = \frac{d^n}{du^n} \log \mathbb{T}(u) \bigg|_{u=0} \tag{2.14}$$

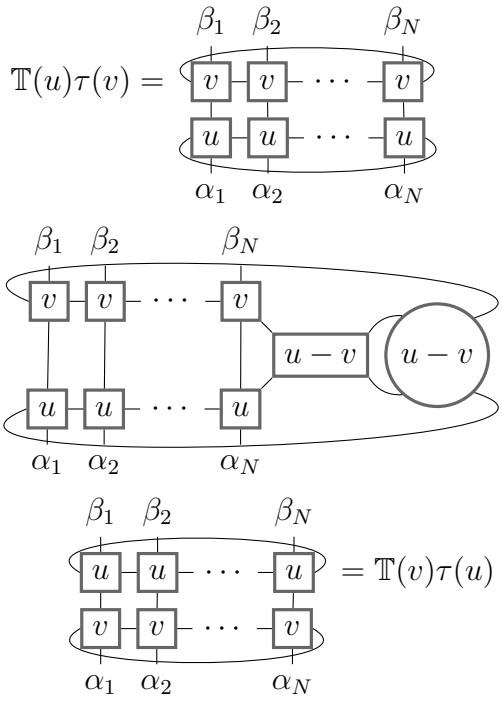

Figure 2.1: Graphical representation of the Yang-Baxter proof of transfer-matrix commutation

up to a normalization, which remain mutually commuting due to the transfer matrix commutation relation [2, 23].

To relate the commuting transfer matrices to the XXZ Floquet circuit, it is necessary to choose a parameterization of the R-matrix such that the corresponding local two-site gate belongs to the same Yang-Baxter family [39]. For an appropriate choice of spectral parameters, the local XXZ gate can be generated from the R-matrix construction, implying that the Floquet circuit inherits the extensive family of conserved operators generated by the transfer matrix. The existence of this extensive family of mutually commuting conserved operators establishes the integrability of the XXZ Floquet circuit [2, 17, 23].

2.3.2 Breaking Integrability

To thermalize the XXZ Floquet circuit, integrability must be broken [10, 13]. To do this, a local impurity λ is introduced to the XX term in a single two-site gate. The non-integrable Floquet unitary is then

$$\tilde{H}^{(j)}_{XXZ} = -T\left(\lambda\sigma^x_j\sigma^x_{j+1} + \sigma^y_j\sigma^y_{j+1} + \Delta\sigma^z_j\sigma^z_{j+1}\right) \tag{2.15}$$

$$U_F = \left(\prod_{j\,\text{even}} e^{-iH^{(j)}_{XXZ}}\right)\left(\prod_{\substack{k\,\text{odd}\\ k>1}} e^{-iH^{(k)}_{XXZ}}\right) e^{-i\tilde{H}^{(1)}_{XXZ}} \tag{2.16}$$

It is important to note that we need to put the error in only a single one of the terms in the Floquet unitary. If we add this defect uniformly to all the terms, it becomes the XYZ circuit, which can be integrable for special choices of λ [21]. We can control the strength of the impurity by changing the values of λ, with values of λ farther from 1 corresponding to stronger impurities and faster thermalization.

This can be seen by examining the local two-site Hamiltonian. In the spin basis $\{|\uparrow\uparrow\rangle, |\uparrow\downarrow\rangle, |\downarrow\uparrow\rangle, |\downarrow\downarrow\rangle\}$ the local Hamiltonian is

$$H^{(i)}_{XXZ} = -T\begin{bmatrix}\Delta & 0 & 0 & 0\\ 0 & -\Delta & 2 & 0\\ 0 & 2 & -\Delta & 0\\ 0 & 0 & 0 & \Delta\end{bmatrix} \tag{2.17}$$

while the Hamiltonian with the impurity becomes

$$\tilde{H}^{(i)}_{XXZ} = -T\begin{bmatrix}\Delta & 0 & 0 & \lambda-1\\ 0 & -\Delta & \lambda+1 & 0\\ 0 & \lambda+1 & -\Delta & 0\\ \lambda-1 & 0 & 0 & \Delta\end{bmatrix} \tag{2.18}$$

The original XXZ Hamiltonian preserves total magnetization, and therefore has the block-diagonal six-vertex structure required by the Yang-Baxter construction [2, 14, 23]. In particular, the only off-diagonal elements allowed are $|\uparrow\downarrow\rangle \leftrightarrow |\downarrow\uparrow\rangle$ which preserves total magnetization. With the impurity, however, the matrix is no longer block-diagonal, and breaks the conservation of total magnetization as it now allows the off-diagonal elements $|\uparrow\uparrow\rangle \leftrightarrow |\downarrow\downarrow\rangle$. Equivalently, this can be stated as $\left[\tilde{H}^{(i)}_{XXZ}, S^z_{\text{tot}}\right] \neq 0$.

As a result, the modified gate no longer satisfies the six-vertex structure underlying the XXZ transfer matrix construction shown above, and therefore no longer

belongs to the same Yang-Baxter family [2, 23]. This destroys the exact transfer-matrix construction responsible for the extensive set of conserved quantities. The impurity therefore removes the conserved quantities responsible for integrability and allows the system to thermalize [10, 13].

2.4 Initial States and Matrix Product Representation

Matrix Product States (MPS) are an efficient way to represent many weakly entangled quantum many-body states, particularly low-entanglement states [31, 32, 36]. Instead of storing exponentially many amplitudes directly, the coefficients are factorized into products of local tensors connected by auxiliary indices [32,36]. For periodic boundary conditions, the matrix product state is defined as

$$|\Psi\rangle = \sum_{\{s\}} \mathrm{Tr}\left[A_1^{(s_1)} A_2^{(s_2)} \dots A_N^{(s_N)}\right] |s_1 s_2 \dots s_N\rangle \tag{2.19}$$

where each $A_i^{(s_i)}$ is a matrix of dimension $D \times D$. D is known as the bond dimension and controls the amount of entanglement in a state [31,36]. Product states correspond to an MPS where the bond dimension is $D = 1$, while larger bond dimensions allow for increasingly entangled states to be represented efficiently.

The brickwork Floquet circuit studied in this thesis has translational invariance by two sites. Initial states with the same translational structure can therefore be represented using two alternating tensors

$$|\Psi\rangle = \sum_{\{s\}} \mathrm{Tr}\left[A_1^{(s_1)} A_2^{(s_2)} A_1^{(s_3)} A_2^{(s_4)} \dots A_1^{(s_{N-1})} A_2^{(s_N)}\right] |s_1 s_2 \dots s_N\rangle \tag{2.20}$$

Matrix product representations therefore provide a convenient framework for constructing initial states with a controlled entanglement structure [36, 40]. The corresponding tensor operations used to construct the initial states numerically were implemented using the Eigen C++ linear algebra library [18]. In particular, the dimer product states studied later naturally admit compact MPS representations with a bond dimension of two.

Chapter 3

The Numerical Implementation

3.1 State Vector Representation

The Floquet circuits studied in this thesis can be represented in the computational basis [28]. For a system of N spins, the Hilbert space has dimension 2^N, so the state vector contains 2^N complex amplitudes. Storing the full quantum state therefore requires memory that scales exponentially with system size.

For example, a system of 30 spins requires a state vector of size 2^{30}. Using complex numbers represented by pairs of 32-bit floating point values requires approximately 8.5 GB of memory for a single state vector. Due to the structure of the brickwork Floquet circuit with periodic boundary conditions, only even system sizes can be considered. Increasing the system size by two spins therefore increases the memory cost by a factor of four.

The computational basis states are represented as

$$|0\rangle = \begin{bmatrix} 1 \\ 0 \end{bmatrix} \qquad |1\rangle = \begin{bmatrix} 0 \\ 1 \end{bmatrix} \tag{3.1}$$

Multi-spin basis states are therefore constructed through the Kronecker products of the individual spins [28].

$$|0\rangle \otimes |1\rangle = |01\rangle = \begin{bmatrix} 1 \\ 0 \end{bmatrix} \otimes \begin{bmatrix} 0 \\ 1 \end{bmatrix} = \begin{bmatrix} 0 \\ 1 \\ 0 \\ 0 \end{bmatrix} \tag{3.2}$$

The tensor-product structure allows the computational basis to be indexed efficiently using binary bitstrings. This makes the local two-site gates naturally compatible with bitwise operations. Since the Floquet evolution is generated entirely from local two-site gates, the dynamics can be implemented through repeated sparse updates of the state vector rather than explicit construction of the full Floquet unitary.

3.2 GPU Parallelization

The Floquet circuits studied in this thesis are simulated through exact state-vector evolution. The most direct implementation would explicitly construct the full Floquet unitary U_F and evolve the state through repeated matrix multiplication

$$|\psi(t)\rangle = U_F^t \, |\psi_0\rangle \tag{3.3}$$

However, this approach is computationally infeasible for large systems. For a system of 30 spins, the Floquet unitary would have dimension $2^{30} \times 2^{30}$, requiring approximately 9×10^3 petabytes of memory to store explicitly. Instead, the locality of the brickwork Floquet circuit allows the dynamics to be implemented entirely through local two-site gate updates [17].

As discussed in Sec. 2.3, the Floquet unitary factorizes into products of local two-site gates. By exploiting this structure, each local gate is applied independently to a small subsystem of the Hilbert space. For a subsystem A containing the spins acted on by a local gate, the Hilbert space is decomposed into

$$A = \{s_a, \ldots, s_b\}, \qquad \bar{A} = \{s_i \,|\, s_i \notin A\} \tag{3.4}$$

where $\bar{A}$ denotes the complement subsystem. An arbitrary state can then be written as [28]

$$|\psi\rangle = \sum_{s_A, s_{\bar{A}}} c_{s_A, s_{\bar{A}}} \, |s_A\rangle \otimes |s_{\bar{A}}\rangle \tag{3.5}$$

A local operator acting only on subsystem A therefore takes the form

$$O_A = O \otimes \mathrm{id}_{\bar{A}} \tag{3.6}$$

so the update acts non-trivially only on the local subsystem while leaving the remaining spins unchanged.

For a two-site gate, the update requires iterating over all 2^{N-2} configurations of the complement subsystem $\bar{A}$. For each fixed configuration $S_{\bar{A}}$, the corresponding four

amplitudes associated with the two-spin subsystem are collected into a local vector,

$$\psi(S_{\bar{A}}) = \begin{bmatrix} \psi_{00,S_{\bar{A}}} \\ \psi_{01,S_{\bar{A}}} \\ \psi_{10,S_{\bar{A}}} \\ \psi_{11,S_{\bar{A}}} \end{bmatrix} \tag{3.7}$$

Then, the local two-site unitary is applied to this four-dimensional vector, and the updated amplitudes are written back into the global state vector. Since each configuration of $\bar{A}$ is disjoint, these updates are embarrassingly parallel and therefore highly suited to GPU parallelization [29].

A simplified implementation of the local two-site update is shown below. This is explicitly the case where the two selected spins are neighbors and not the first and last spin. The bitwise indexing identifies the four amplitudes associated with a fixed configuration of the complement subsystem. It then applies the local unitary and updates the amplitudes in the global state vector.

```
size_t c0=(i&mask)+((i&~mask)<<2);
size_t c1=c0+s1;
size_t c2=c0+s2;
size_t c3=c0+s1+s2;

complex<float> v0=psi[c0];
complex<float> v1=psi[c1];
complex<float> v2=psi[c2];
complex<float> v3=psi[c3];

psi[c0]=U[0]*v0+U[1]*v1+U[2]*v2+U[3]*v3;
psi[c1]=U[4]*v0+U[5]*v1+U[6]*v2+U[7]*v3;
psi[c2]=U[8]*v0+U[9]*v1+U[10]*v2+U[11]*v3;
psi[c3]=U[12]*v0+U[13]*v1+U[14]*v2+U[15]*v3;
```

The state vector is stored directly in the computational basis, where each basis state corresponds to a binary string of length N. This makes mapping between a spin configuration and its array straightforward, since each bitstring is itself an integer in base two. As a result, local gate updates can be implemented efficiently using bitwise indexing rather than constructing the full Floquet unitary.

This structure is naturally suited to the GPU. The full state vector can be kept in

global GPU memory along with the local two-site unitary, with each thread processing one independent subsystem configuration and applying the corresponding local gate update. For each two-site unitary, all subsystems are disjoint, so there are no race conditions, and each thread does not have to check if it can access its elements. This is what makes the algorithm embarrassingly parallel. Since the operations are extremely simple, they can be executed simultaneously with single-instruction multiple-thread (SIMT) execution [29]. This allows for the classical simulation of up to 30 spins on consumer-grade laptops.

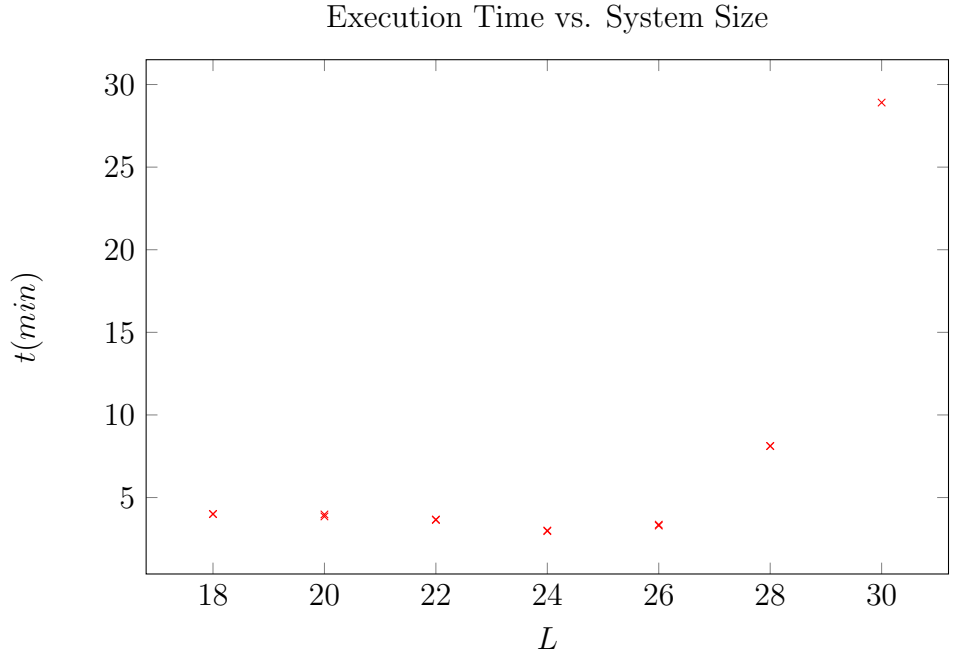

Figure 3.1: Execution Speed for 1000 Iterations

3.3 Code Performance

As discussed in the previous section, the code is embarrassingly parallel, allowing for substantial acceleration through GPU parallelization [29]. Fig. 3.1 shows the execution times of the program for two representative simulations with different initial states. The execution time of the program is not affected by the initial parameters or states and remains approximately constant up to 24 spins, after which the runtime increases rapidly with system size. The exponential increase is expected, since the state vector increases by a factor of four each time the system size increases by two. The constant execution time for up to 24 spins suggests that kernel launch overhead and memory access overhead dominate the runtime [29, 30]. This is logical, since at these times each thread only runs for a few iterations.

The main bottleneck is the amount of VRAM on the GPU. Since the system can only be an even number of spins, each increase grows the needed VRAM by a factor of four. For 32 spins, that would be around 35 gigabytes of data. This is only available on high-end GPUs. The best workaround is to stream portions of the state vector between host and device memory [29, 30]. This is only beneficial if the computation takes longer than copying the data from the CPU to the GPU; however, local gate updates are sufficiently lightweight that host-device transfer dominates the runtime. This limits accessible sizes to systems of up to 30 spins.

3.4 Numerical Stability and Finite-Size Limitations

Although the simulations in this thesis are performed using exact state-vector evolution, alternative approaches to efficient simulation have been investigated. Approaches that are based on tensor-network methods can often simulate one-dimensional quantum systems more efficiently by exploiting the low-entanglement structure of many-body states [8, 40]. For generic non-integrable Floquet circuits, however, entanglement entropy is expected to grow rapidly, making tensor-network truncation inefficient [3, 27]. Therefore, exact state-vector evolution is the best controlled framework for studying thermalization dynamics of the Floquet circuit considered here.

The following numerical simulations are performed through the exact state-vector evolution in the computational basis. This is done by exploiting the structure of the brickwork Floquet circuit to efficiently implement the dynamics through repeated application of the local two-site operators. Although this is vastly more efficient than explicitly calculating the full Floquet unitary, it still scales exponentially with system size. Therefore, both accessible system sizes and evolution times are computationally constrained.

Although GPU acceleration allows the simulations to reach system sizes and timescales that would otherwise be inaccessible, the accessible system sizes are still constrained. Consequently, the results should be interpreted as finite-size numerical evidence for the thermalization dynamics of weakly non-integrable Floquet circuits rather than definitive asymptotic thermodynamic scaling results. The accessible system sizes, however, are nevertheless sufficient to observe the crossover from constrained dynamics in the integrable regime to the infinite temperature limit once the impurity is introduced.

The data were generated using 32-bit floating point precision. Single precision was chosen to best take advantage of GPU parallelization, as in many consumer GPUs, double precision arithmetic is throttled [29]. Therefore, precision is sacrificed to allow for larger accessible systems.

While the Floquet evolution is itself unitary, the floating point arithmetic introduces numerical rounding errors [16]. Therefore, the norm of the quantum state can drift away from unity. Numerical precision errors can therefore provide a direct measure of the stability of the implementation. Over the accessible simulation times, the norm drift remained negligible.

Chapter 4

Numerical Results

4.1 Physical Observables and Diagnostics

In the integrable regime, local observables associated with conserved quantities remain constrained throughout the dynamics. These observables therefore provide a natural diagnostic for the persistence of integrability in a system once a local impurity is introduced and thermalization occurs. In the integrable regime, the expectation values either remain constant or fluctuate around nonzero plateau values inherited from the conserved quantities depending on the initial state and the observables.

In this work, we study local magnetization, average magnetization, two-point magnetization, and bond observables. These are natural probes of the XXZ Floquet circuit since the integrable model preserves total magnetization, while the bond observable belongs to the same Yang-Baxter structure as the XXZ interaction itself. The average magnetization and bond observables are defined as

$$\bar{m} = \frac{1}{L}\sum_{i=1}^{L}\sigma_i^z \tag{4.1}$$

$$B_{i,j} = \sigma_i^x\sigma_j^x + \sigma_i^y\sigma_j^y + \Delta\sigma_i^z\sigma_j^z \tag{4.2}$$

Local magnetization is a sensitive single-site probe of thermalization and is comparatively simple to interpret, although it can exhibit strong oscillatory dynamics. Averaging local magnetization can suppress this oscillatory behavior and provide a cleaner diagnostic for the fully polarized state, but vanishes for the other states studied. Bond observables probe short-range correlations between spins and are particularly sensitive to local correlation dynamics, although they are generally noisier and exhibit more oscillatory behavior than single-site observables. In general, observables acting on more than a single-site exhibit more complicated dynamics.

When integrability is broken in the circuit, the expectation values of these observables are no longer constrained by the conserved quantities in the circuit. Therefore, as the system thermalizes, these observables should relax towards their infinite-temperature expectation values. Thermalization is therefore diagnosed through the decay of initially constrained local observables towards the infinite-temperature expectation values.

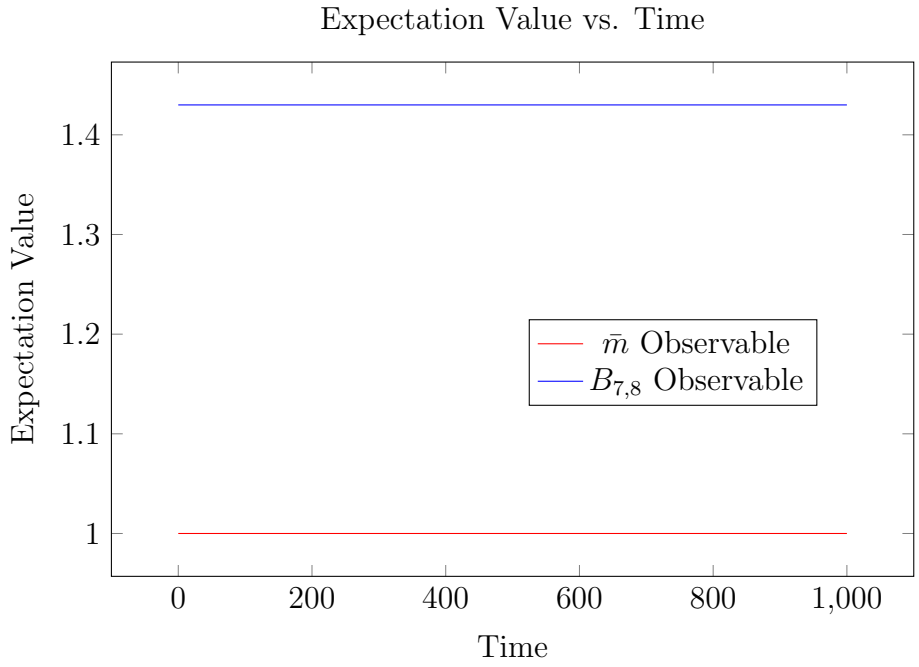

Figure 4.1: Constant expectation values of local observables in the integrable XXZ Floquet circuit for the fully polarized state

4.2 Integrable Dynamics of the XXZ Floquet Circuit

4.2.1 Fully Polarized State

The fully polarized state serves as a simple benchmark state, as it is an eigenstate of the integrable XXZ circuit and therefore has no dynamics. Since the XXZ gates preserve total magnetization, the fully polarized state cannot be mixed with any other basis state under the integrable dynamics. Fig. 4.1 shows constant expectation values for the selected observables, which agrees with the expectation since the fully polarized state is an eigenstate.

All system sizes produce the same constant expectation values throughout the time evolution, consistent with the absence of dynamics in the fully polarized state. Consequently, all the local one-site and two-site magnetization observables collapse onto a single value, as do the bond observables.

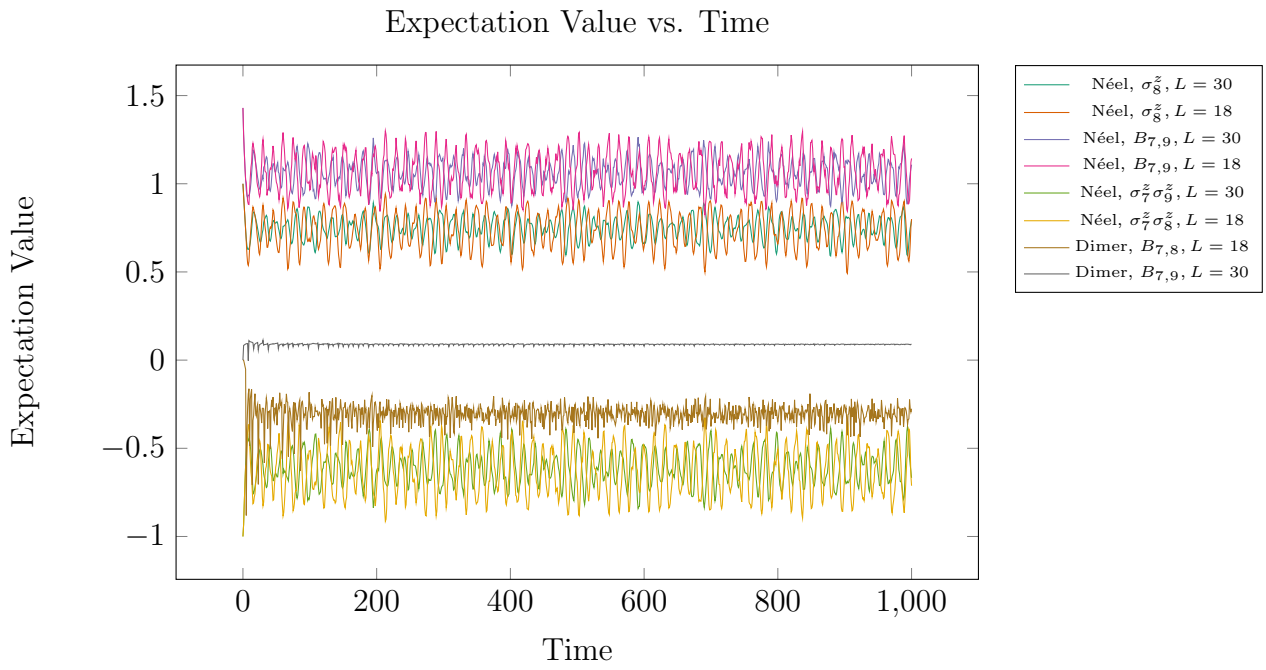

Figure 4.2: Persistent constrained oscillatory dynamics of local observables in the integrable XXZ Floquet circuit for the Néel and dimer product initial states

4.2.2 The Néel and Dimer Product States

The Néel state is a product state of alternating spins. The dimer product state is the tensor product of maximally entangled nearest neighbor Bell pairs. These states are defined as

$$|\text{Néel}\rangle = |0101\ldots\rangle \tag{4.3}$$

$$|\text{Dimer}\rangle = \bigotimes_{j=1}^{N/2} \frac{|01\rangle_{2j,2j+1} - |10\rangle_{2j,2j+1}}{\sqrt{2}} \tag{4.4}$$

Neither of these states are eigenstates of the XXZ circuit, and therefore experience nontrivial dynamics without thermalizing. The local observables oscillate around nonzero plateau values that are constrained by the conserved quantities in the circuit. Fig. 4.2 shows persistent oscillatory dynamics around nonzero plateau values for a variety of observables, consistent with the constrained dynamics of the integrable XXZ circuit.

The integrable XXZ Floquet circuit therefore exhibits nonthermal dynamics across

all studied initial states due to the extensive conserved quantities in the Floquet unitary. While the fully polarized state remains completely stationary due to being an exact eigenstate, the Néel and dimer product states display persistent oscillatory dynamics around nonzero expectation values that are constrained by the conserved quantities of the integrable circuit. These nonzero plateaus for the selected observables provide a baseline in which the behavior of systems with a single non-integrable impurity can be compared.

4.3 Thermalization Induced by a Local Impurity

To break the integrability of the XXZ Floquet circuit, a single local impurity is introduced between the first and second spins by modifying the $\sigma^x\sigma^x$ coupling with a scaling parameter $\lambda = 1$. This single impurity breaks the integrability of the Floquet circuit and ultimately leads to thermalization. Fig. 4.3 shows the decay from the nonzero constrained expectation value towards the infinite-temperature plateau. The size of the impurity can be controlled by fine-tuning the impurity parameter λ. It is shown in Fig. 4.3 that impurities closer to the integrable value of $\lambda = 1$ produce slower thermalization dynamics.

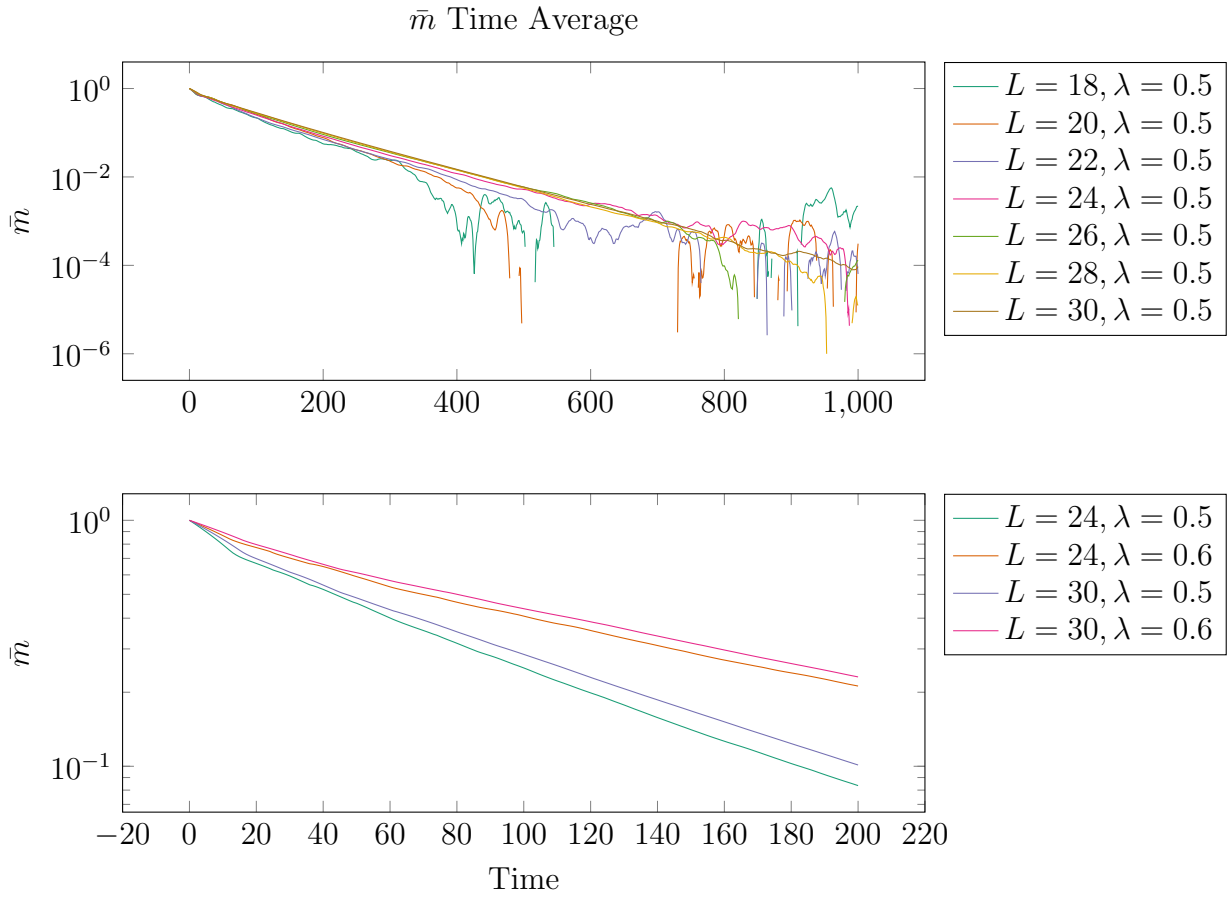

Figure 4.3: Decay of $\bar{m}$ in the fully polarized state once a single non-integrable impurity is placed in the otherwise integrable XXZ Floquet circuit

Since the system is local, the decay spreads ballistically through the system. The locality enforced by the brickwork structure of the Floquet circuit imposes a speed

limit on how fast the non-integrability can spread through the system. The delayed onset of the infinite-temperature plateaus for larger system sizes suggests that the impurity-induced thermalization timescale grows with system size.

The thermalization behavior is consistent across all the initial states. Fig. 4.4 shows this behavior; however, these decays are less clear. This is due to the use of a single-site observable, as the total magnetization vanishes for the Néel state. The monotonic increase in decay times still emerges at late times despite the strong oscillatory behavior.

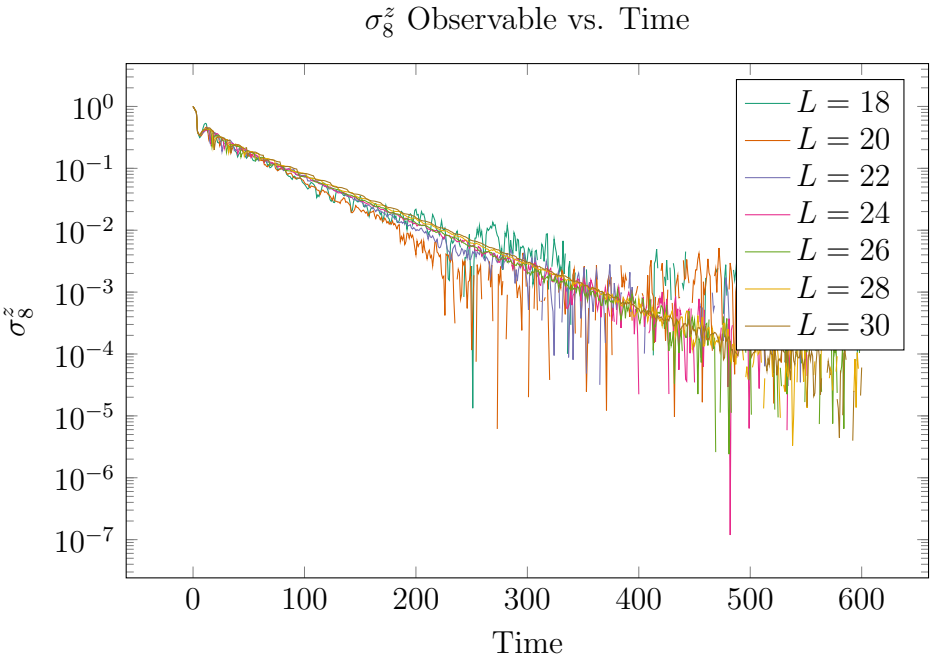

Figure 4.4: Decay of σ_8^z in the Néel state once a single non-integrable impurity is placed in the otherwise integrable XXZ Floquet circuit for $\lambda = 0.5$

The dimer product state exhibits more complicated dynamics between the spins due to initial short-range entanglement structure. Although the decay rates are less visually separated across system sizes than in the fully polarized state, the onset of the late-time plateau still monotonically increases with system size. This again suggests that larger system sizes are correlated with longer thermalization timescales despite the transient dynamics.

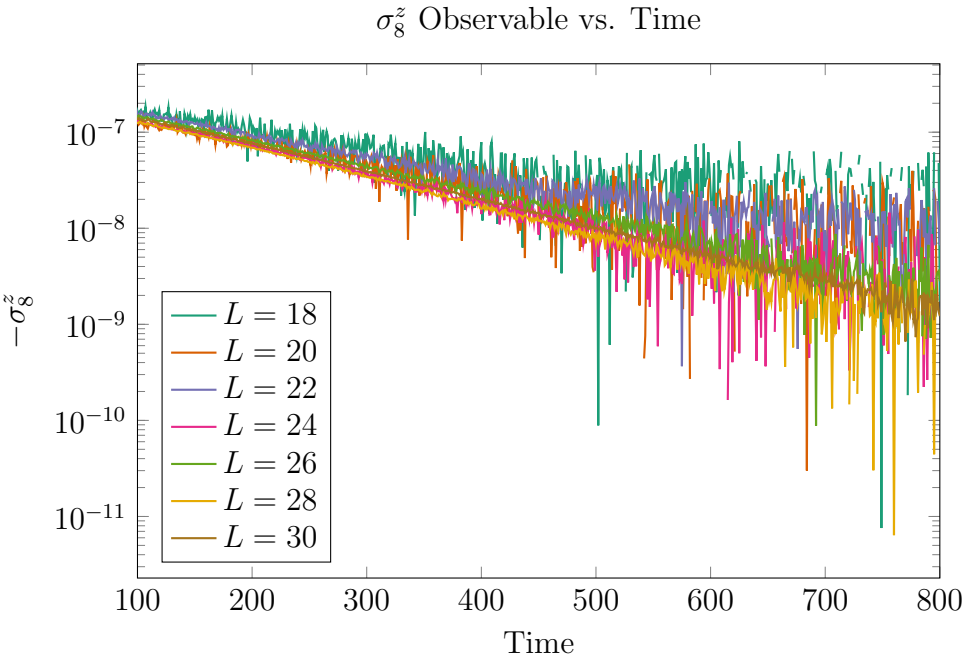

Figure 4.5: Decay of σ_8^z in the dimer product state once a single non-integrable impurity is placed in the otherwise integrable XXZ Floquet circuit for $\lambda = 0.5$

While the detailed decay dynamics depend strongly on both the initial state and the observables, all studied states exhibit increasing thermalization timescales with increasing system size. The fully polarized state provides the clearest example of this due to the lack of initial dynamics, although the same qualitative trend remains visible in both the Néel and dimer product states.

4.4 Extracting Thermalization Timescales

Thermalization in finite-size Floquet systems with a single impurity is not associated with a sharply defined transition into the infinite-temperature regime. Therefore, multiple diagnostics are required to extract characteristic thermalization timescales. The observed dynamics of the decays not only contain contributions from the heating introduced by the impurity, but also from the constrained dynamics of the rest of the circuit.

Many observables exhibit approximately linear behavior on logarithmic plots during the early-time regime. Therefore, a natural way to characterize the decays is to fit a standard exponential to this region and compare the decay coefficients. The resulting decay coefficients can then be used as an effective measure of the early-time thermalization rate. These early-time fits, however, primarily probe the local dephasing dynamics generated by the impurity rather than the total thermalization of the circuit.

A second diagnostic is obtained by time averaging the observables to suppress the oscillatory dynamics of the circuit. If the observed early-time scaling is robust, the time-averaged observables should exhibit similar scaling behavior for the early-time regime. The late-time behavior of the time-averaged observables is also examined.

A complementary diagnostic defines thermalization time through the onset of the late-time plateau regime. The plateau-entry time is defined as the first time for which the observable remains within

$$|O(t) - O_{plateau}| \leq n\sigma \tag{4.5}$$

of the late-time plateau value. Unlike the early-time exponential fits, this diagnostic probes the late-time behavior at the level of late-time observable fluctuations, and therefore may capture different aspects of the thermalization dynamics.

4.4.1 Early-time Decay Fits

When plotting the raw decays on a log-plot, the decays look approximately linear. This suggests that a good model of the decay is a standard exponential in the early-time regime. Therefore, a standard exponential of the form

$$f(t) = A\exp[-t/\tau] + C \tag{4.6}$$

is fit.

The fitting window is chosen in the region where the decays appear approximately linear on logarithmic plots across all system sizes. This starts occurring at around $t \approx 50$ and may extend to $t \approx 600$ depending on the initial parameters and the chosen observables used. The representative exponential fits in the early-time regime of the decays are shown in Fig. 4.6.

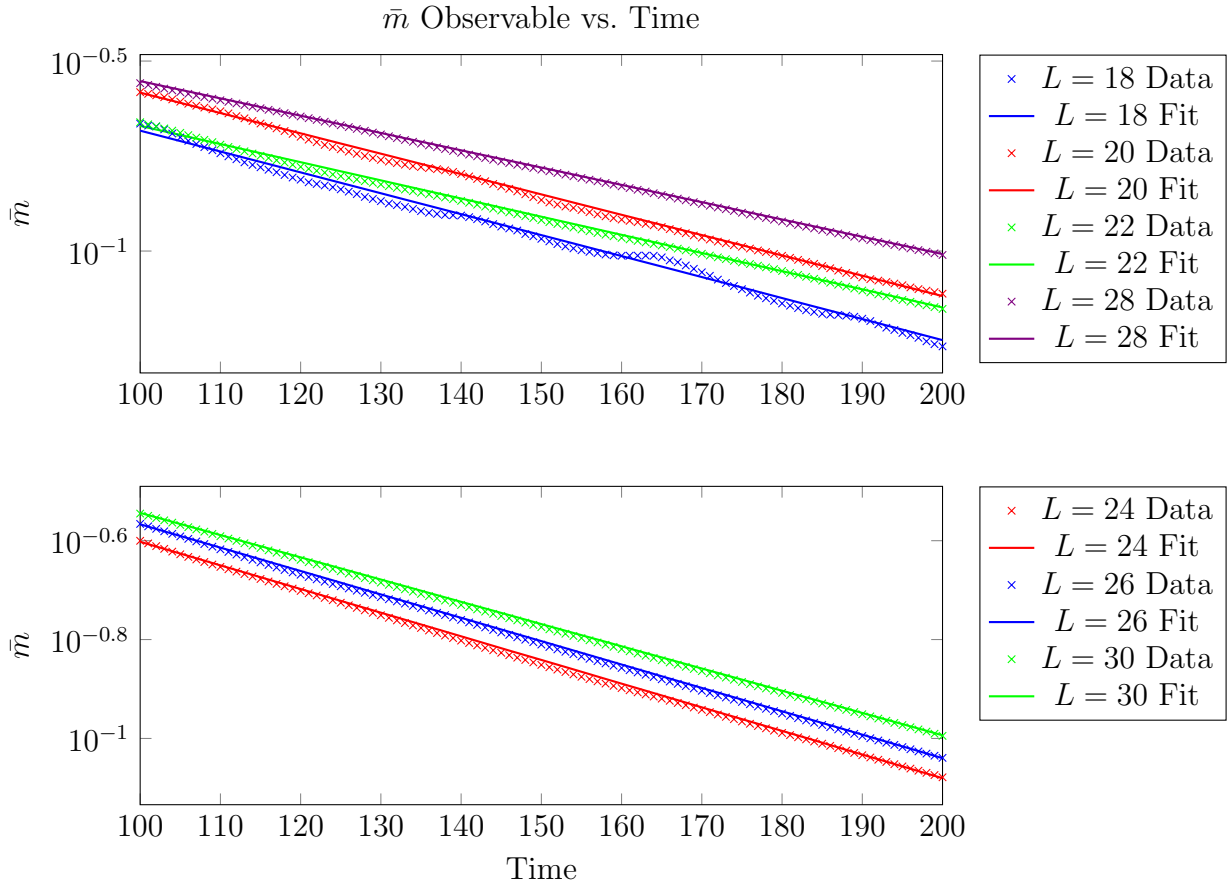

Figure 4.6: Early-time decays with standard exponential fits for $\bar{m}$ for the fully polarized state for $\lambda = 0.5$

Approximate linear early-time behavior on logarithmic plots appears consistently across multiple initial states and impurity strengths. Fig. 4.7 shows the fits for a smaller error, which also has the linear decays on a log-plot for a later time scale of $t = 400$ to $t = 600$.

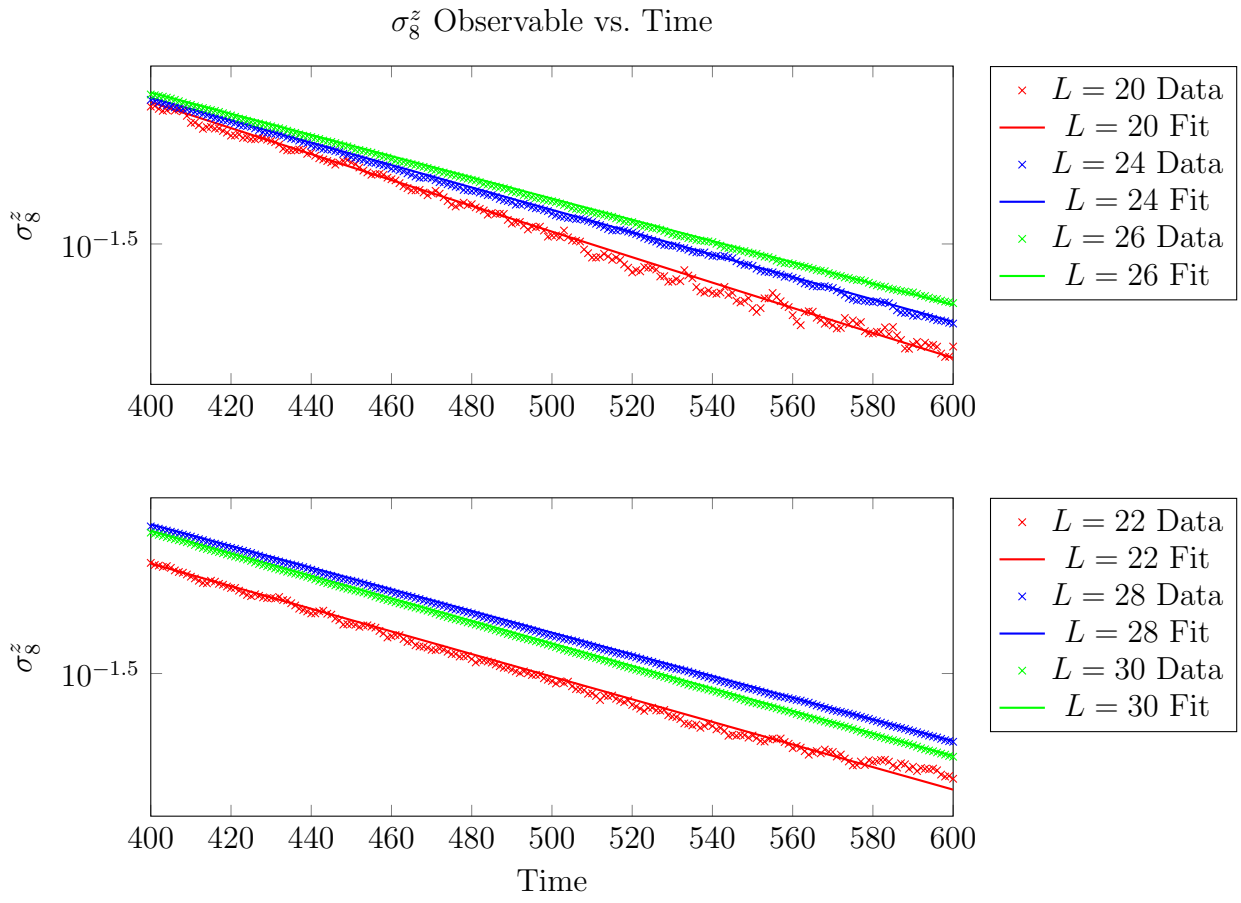

Figure 4.7: Early-time decays with standard exponential fits for $\bar{m}$ for the fully polarized state for $\lambda = 0.6$

The linear region on a log-plot shows up consistently with the other initial states. In Fig. 4.8 and Fig. 4.9, the linear regions of the decays are plotted and fitted for the different system sizes.

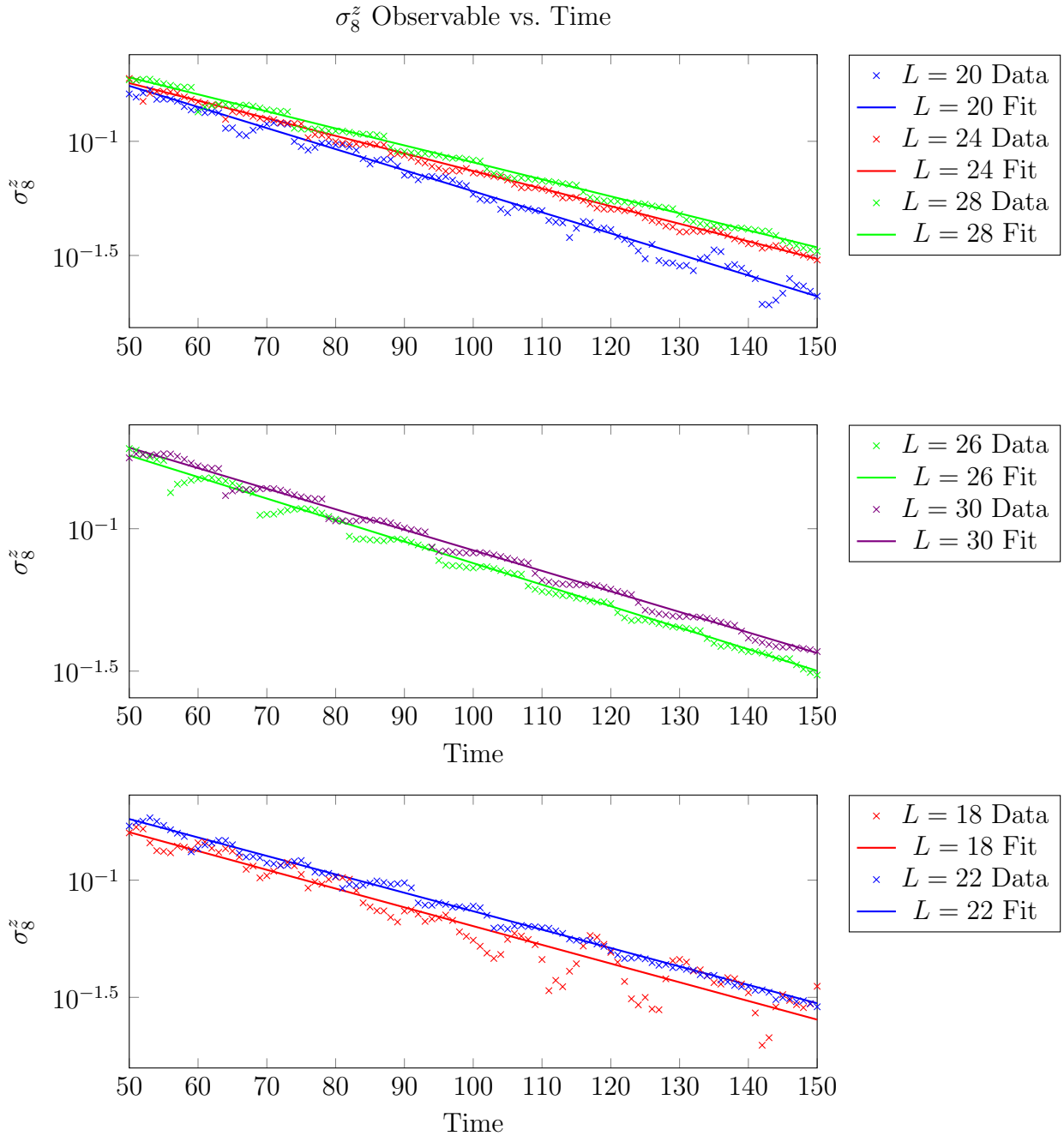

Figure 4.8: Early-time decays with standard exponential fits for σ_8^z for the Néel state for $\lambda = 0.5$

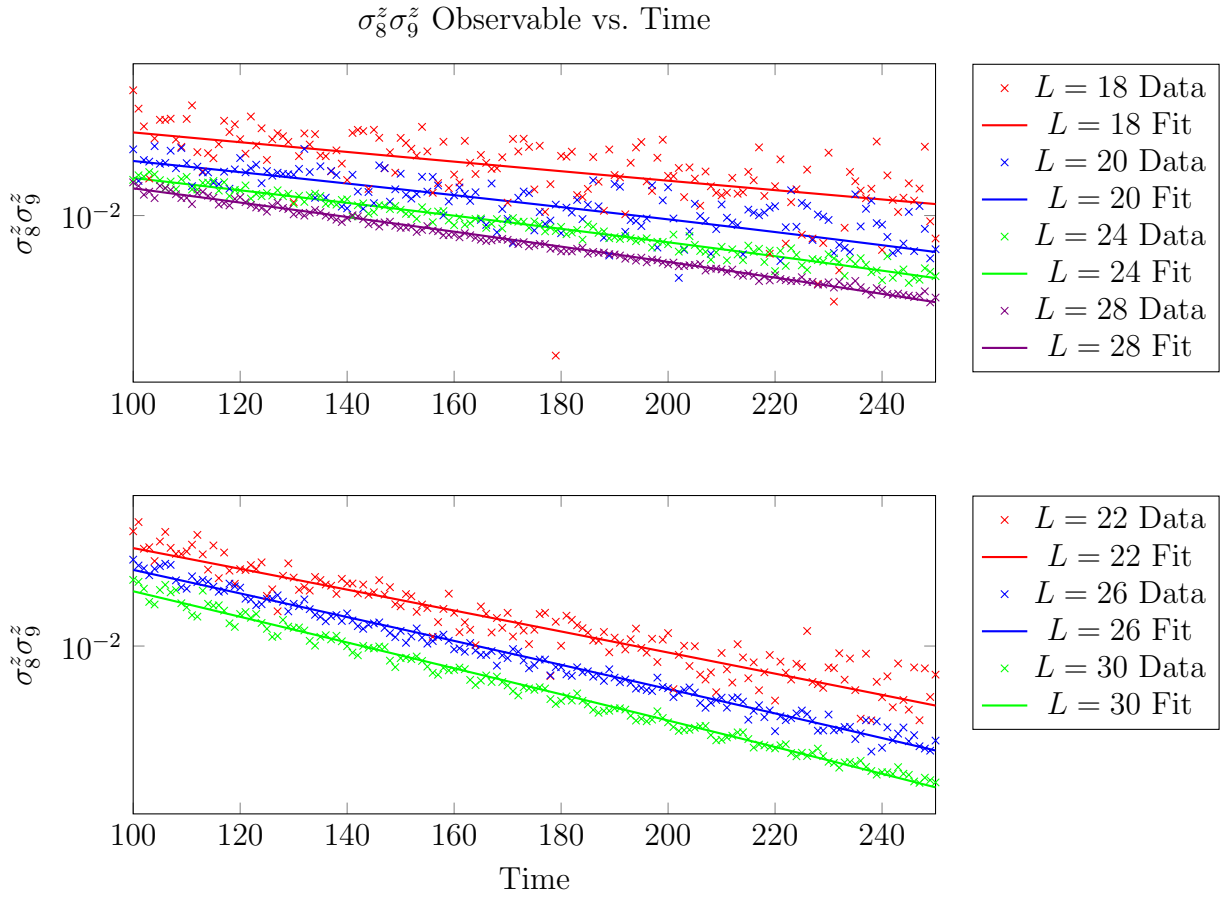

Figure 4.9: Early-time decays with standard exponential fits for $\sigma_8^z\sigma_9^z$ for the dimer product state for $\lambda = 0.5$ with a sign flip

While the exponential fits provide a useful characterization of the early-time decay dynamics, the extracted decay coefficients exhibit strong dependence on both the initial state and the chosen observable. The scaling behavior of these coefficients is examined in the following section.

4.4.2 Extracted Early-Time Decay Times

In the standard exponential fits, comparing the decay parameter τ is equivalent to comparing decay times. Fig. 4.10 and Fig. 4.11 show a linear relationship between the decay time and the system size. This is an interesting result, as it suggests that rapid local dephasing occurs once the impurity reaches a site. One possible interpretation of the approximately linear scaling is that the impurity emits dephasing fronts that propagate ballistically through the circuit, limited in speed by the locality of the circuit. After a timescale proportional to the system size, the local observable will have experienced repeated dephasing events introduced by the impurity. The extracted early-time decay time may therefore probe local dephasing dynamics rather than the overall thermalization of the full system.

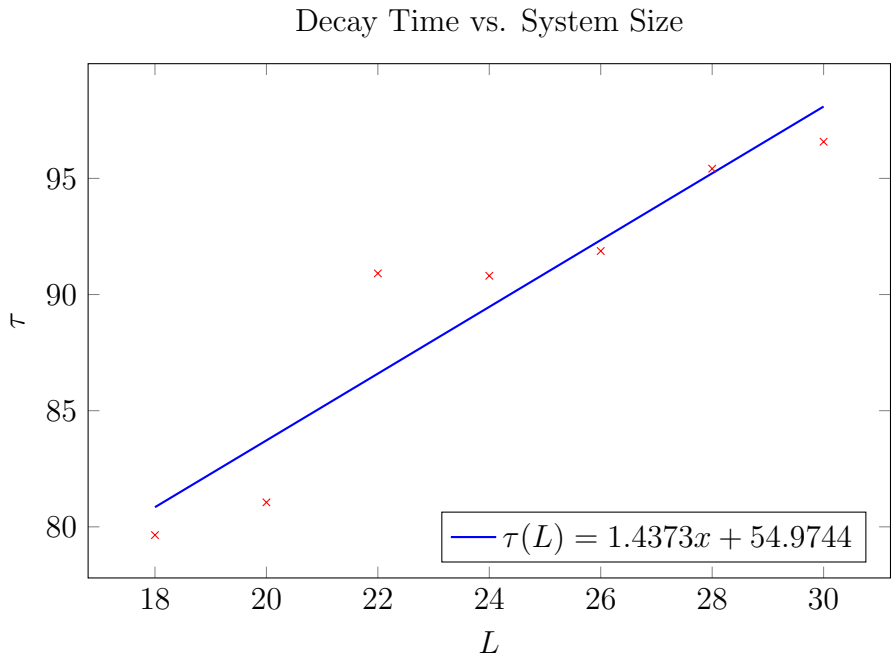

Figure 4.10: Decay time τ vs. system size of $\bar{m}$ for the fully polarized state for $\lambda = 0.5$

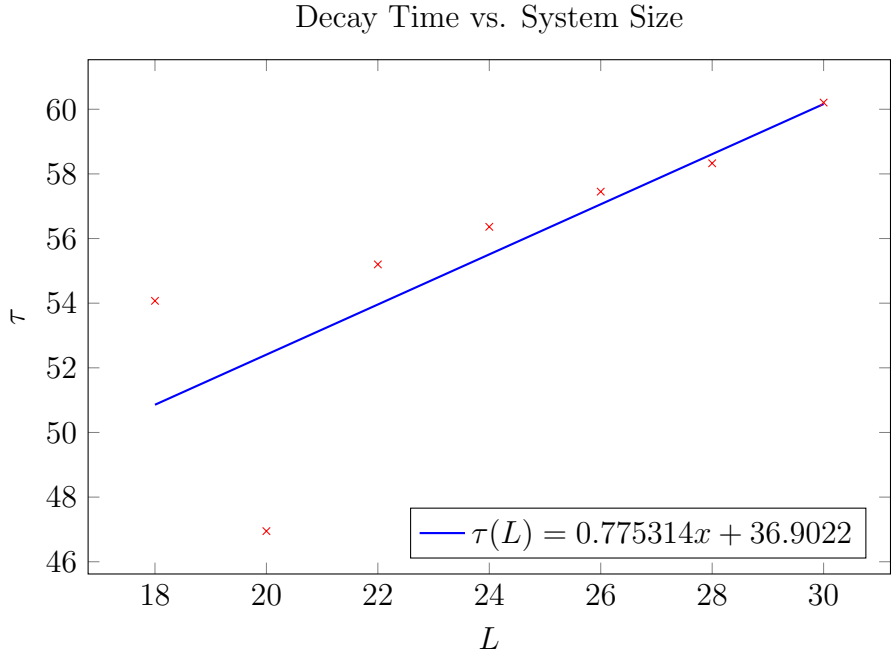

Figure 4.11: Decay time τ vs. system size of σ_8^z for the Néel state for $\lambda = 0.5$

This behavior is not universally extracted. In fact, the opposite behavior emerges for the $\sigma_8^z\sigma_9^z$ observable on the dimer product state. Fig. 4.12 shows an increasing decay rate with system size, along with an even-odd effect. Since the circuit is translationally invariant by two sites, the extracted decay rates exhibit an even-odd effect distinguishing systems of size $L \mod 4 = 0$ and $L \mod 4 = 2$. The initial state is a tensor product of maximally entangled Bell states, and larger states would include a larger number of entangled dimers. This suggests that the extracted early-time decay rates may reflect the local scrambling of the entanglement structure rather than the global thermalization timescale.

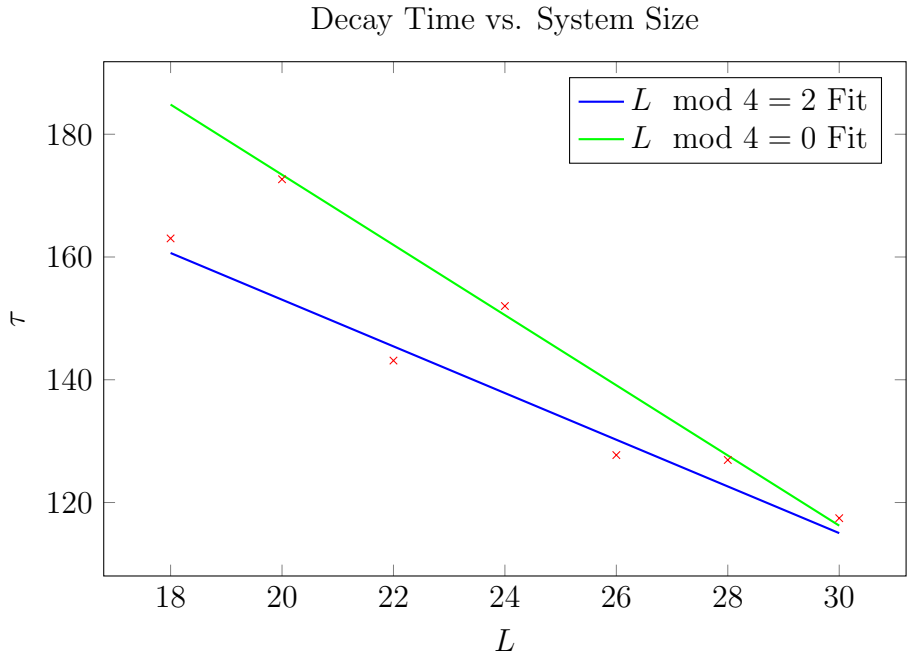

Figure 4.12: Decay time τ vs. system size of $\sigma_8^z \sigma_9^z$ for the dimer product state for $\lambda = 0.6$

The relationship between the extracted decay times and the system size can not always be clearly seen. Fig. 4.13 shows the extracted decay time for the fully polarized state for $\lambda = 0.6$, and the extracted decay times exhibit a weak but non-monotonic increase with system size. This provides more evidence for the decay in the early-time regime probing the local scrambling dynamics rather than full thermalization, as the full decay profiles still exhibit systematically delayed plateau formation with system size.

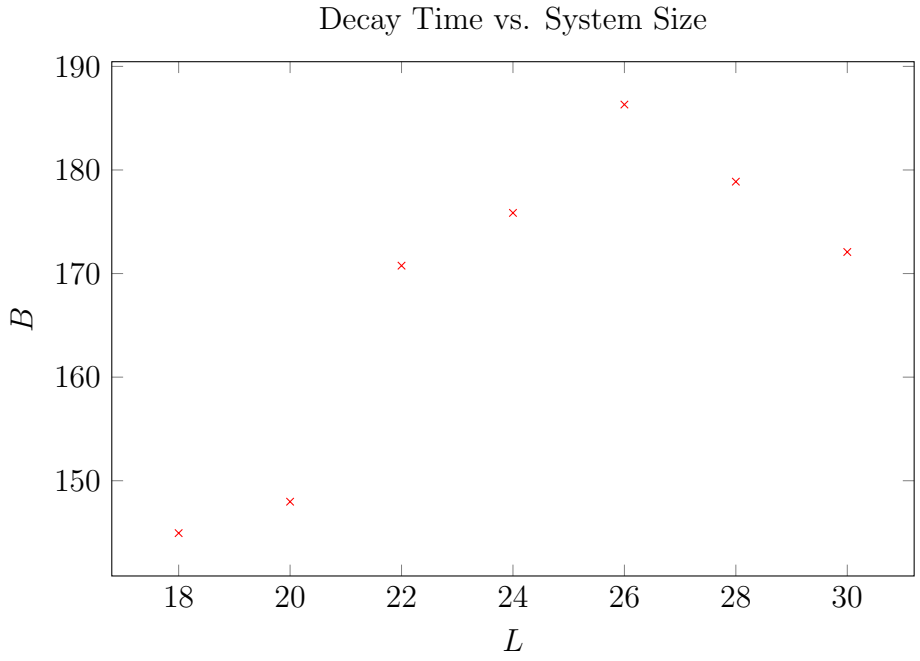

Figure 4.13: Decay time τ vs. system size of the average magnetization for the fully polarized state for $\lambda = 0.6$

The extracted decay times are sensitive to the chosen initial state and observable. While several observables display approximately linear scaling with system size, other observables exhibit non-monotonic or even opposite trends. This strongly suggests that the early-time decay reflects the local impurity induced dephasing dynamics rather than the global thermalization timescale.

4.4.3 Time-Averaged Dynamics

In periodically driven systems, instantaneous expectation values generally exhibit oscillatory behavior inherited from underlying dynamics of the circuit. This can make it difficult to extract a characteristic thermalization timescale, as oscillations complicate extracting the underlying decay dynamics. Time averaging suppresses these oscillations while preserving the overall relaxation behavior.

The time-averaged observable is defined as

$$\bar{O}(T) = \frac{1}{T}\int_0^T O(t)dt \tag{4.7}$$

where $O(t)$ denotes the observable being measured. For discrete numerical data, this becomes

$$\bar{O}(T) = \frac{1}{T}\sum_{t=0}^{T} O(t) \tag{4.8}$$

Unlike the raw observables, time-averaged quantities are less sensitive to transient oscillatory dynamics, and can therefore provide a cleaner probe of the relaxation behavior. Comparing extracted timescales from the early-time regime of the time-averaged decays allows us to determine whether the scaling obtained from raw observables is robust or dominated by the oscillatory dynamics inherited from the circuit.

4.4.3.1 Full Time-Averaged Decays

The full time-averaged decay of the average magnetization in the fully polarized state at $\lambda = 0.6$ is shown in Fig. 4.14. Time averaging suppresses the oscillatory dynamics, making the overall relaxation trend easier to identify. The early-time regime of the raw decays appears exponential with oscillations. If the decay mechanism is robust, the same effect should persist in the early-time regime of the time average. In the late-time regime, larger systems appear approximately linear on a log-log plot. This suggests that these systems may be governed by a power-law at late times. The time-averaged dynamics therefore appear to exhibit qualitatively distinct early-time and late-time relaxation regimes.

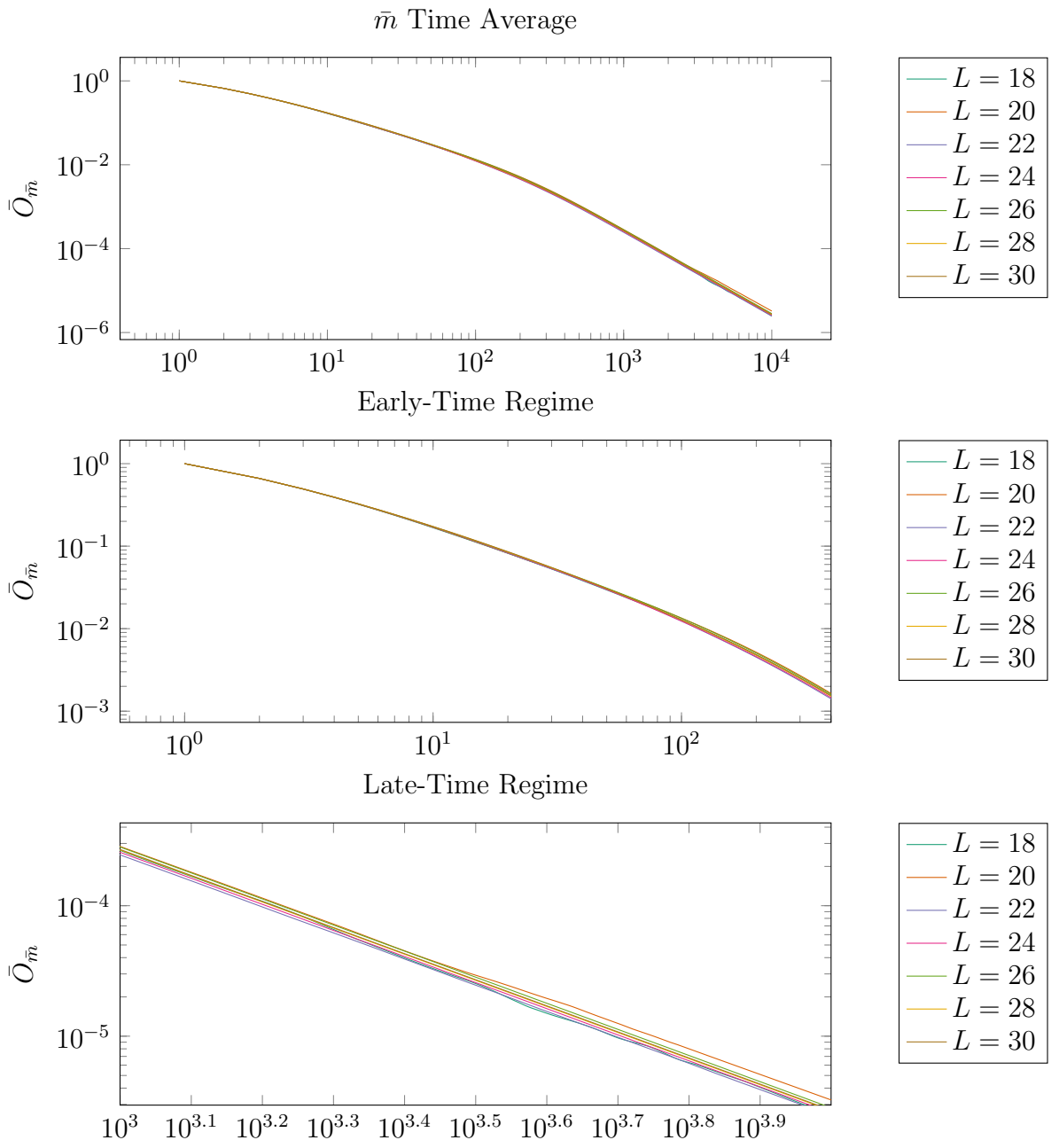

Figure 4.14: Time-averaged decay of $\bar{m}$ for the fully polarized state for $\lambda = 0.6$

4.4.3.2 Early-Time Time-Averaged Scaling

The early-time regime of the raw decays appears approximately exponential with fluctuations. This means that the early-time regime should be well fit by

$$\frac{A}{x}\exp[-x/B] + C \tag{4.9}$$

at similar time regimes to the raw decays. Fig. 4.15 shows the early-time regime exponential fits of the time-averaged expectation value of the average magnetization for the fully polarized state for $\lambda = 0.5$.

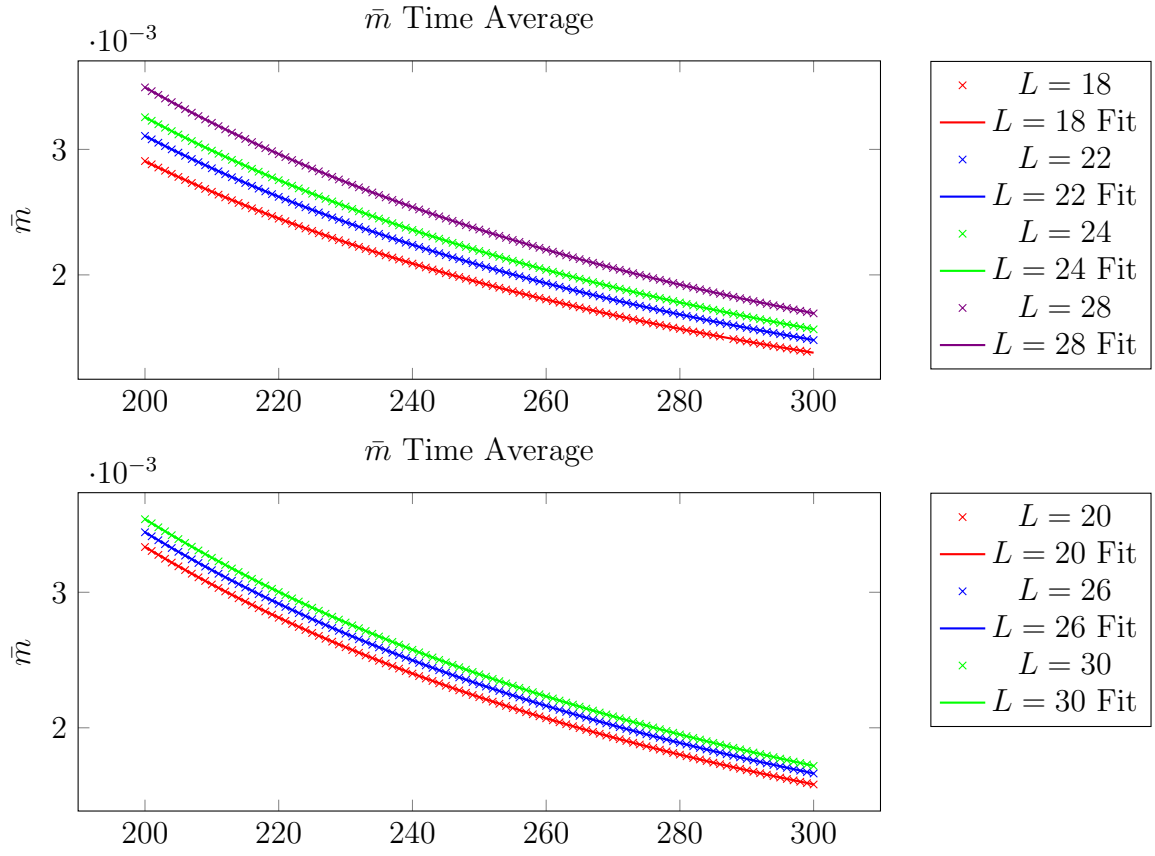

Figure 4.15: Time average of $\bar{m}$ in the fully polarized state for $\lambda = 0.5$

The decay times extracted from the fits and plotted in Fig. 4.16 exhibit an approximately linear relationship between decay time and system size. This suggests that the relationship between the early-time regime decay time and system size is robust under fluctuations in the raw decay.

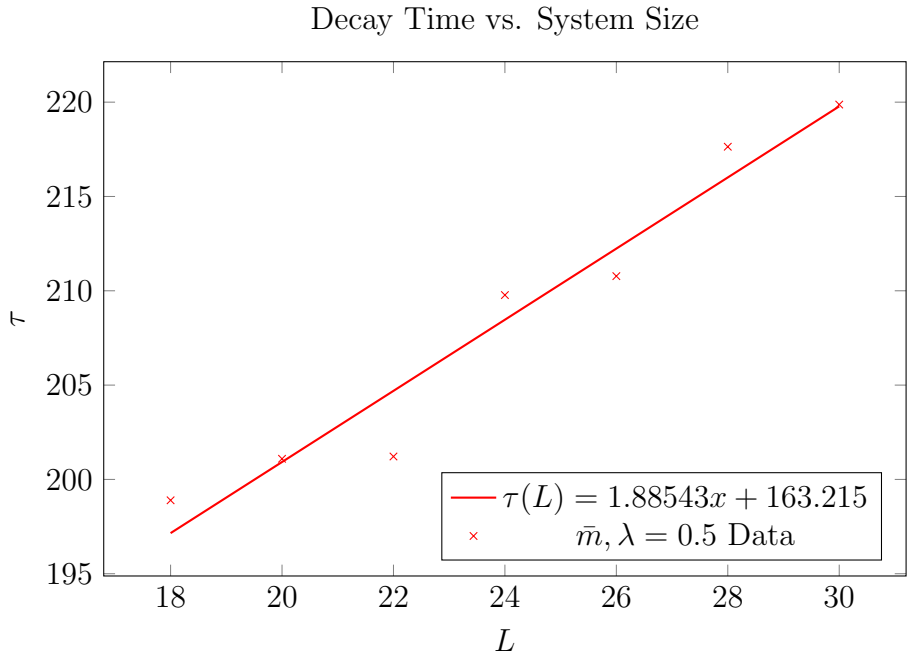

Figure 4.16: Extracted decay time in the early-time regime for time-averaged $\bar{m}$ in the fully polarized state for $\lambda = 0.5$

The time-averaged decays for the Néel and dimer product states experience qualitatively similar behavior in the early-time as the raw decays. This suggests that the early-time decays are robust under time averaging, but primarily probe local dephasing rather than the global thermalization.

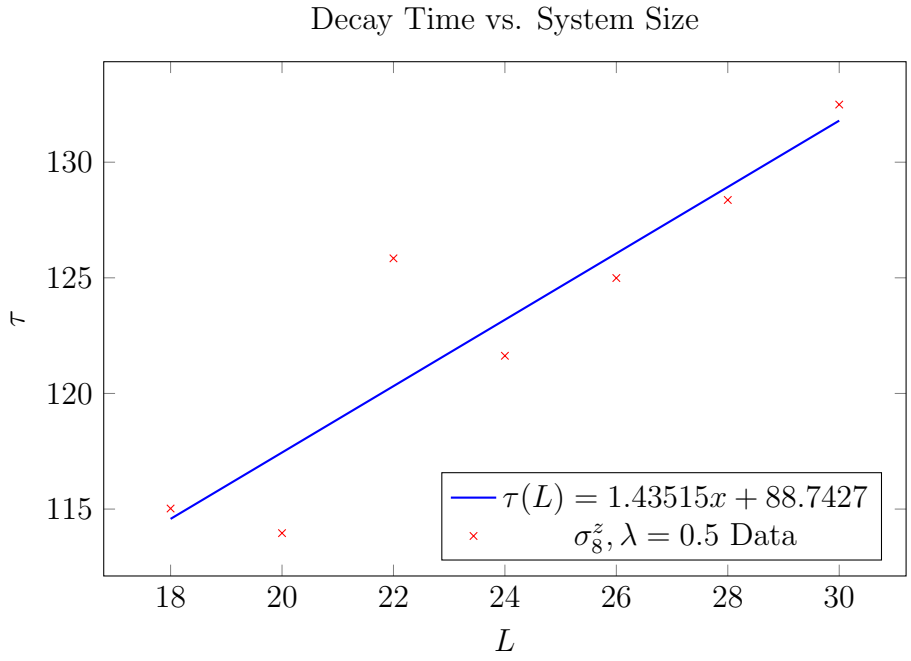

Figure 4.17: Extracted decay time in the early-time regime for time-averaged σ_8^z in the Néel state for $\lambda = 0.5$

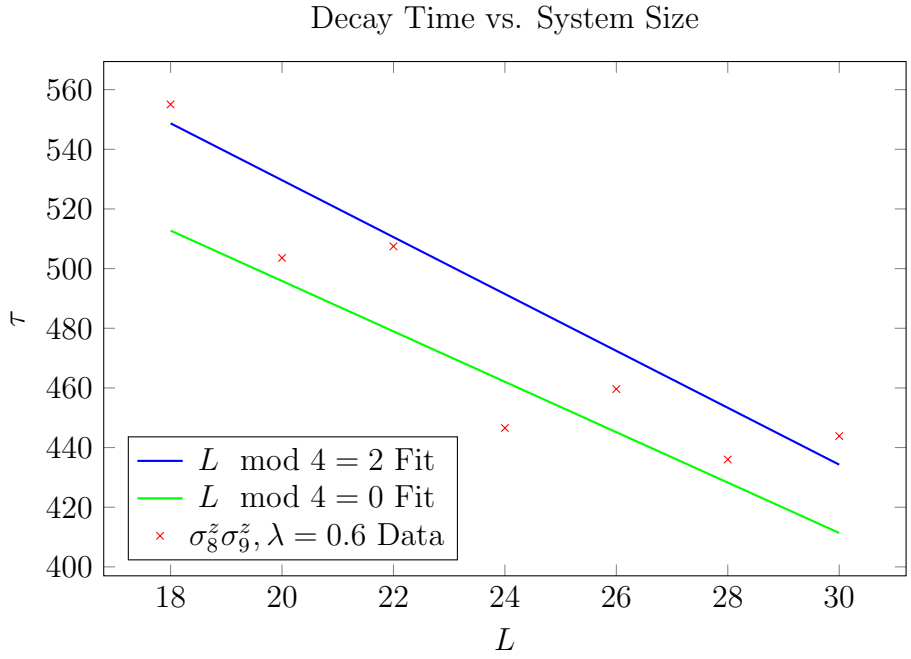

Figure 4.18: Extracted decay time in the early-time regime for time-averaged $\sigma_8^z\sigma_9^z$ in the dimer product state for $\lambda = 0.6$

Time averaging reproduces the same qualitative early-time scaling behavior ob-

served in the raw decays. In particular, the fully polarized and Néel states exhibit approximately linear growth of extracted decay times with system size, while the dimer product state exhibits the opposite behavior. Integrating an exponential decay preserves the characteristic decay timescale, suggesting that early-time scaling is not solely an artifact of oscillatory dynamics in the decay, but rather a probe of local dephasing dynamics.

4.4.3.3 Late-Time Time-Averaged Dynamics

The late-time regime appears approximately linear on a log-log plot which suggests that the late-time regime may be described by a power-law. The decay can be fit with a power-law of the form

$$f(t) = At^{-B} + C \tag{4.10}$$

The fitted exponents were found to vary only weakly across system sizes within the fitting uncertainty. To reduce fitting instability and allow for direct comparison between system sizes, the exponent B was fixed across the fits. As system size increases, the power-law fitted to the late-time regime becomes more accurate.

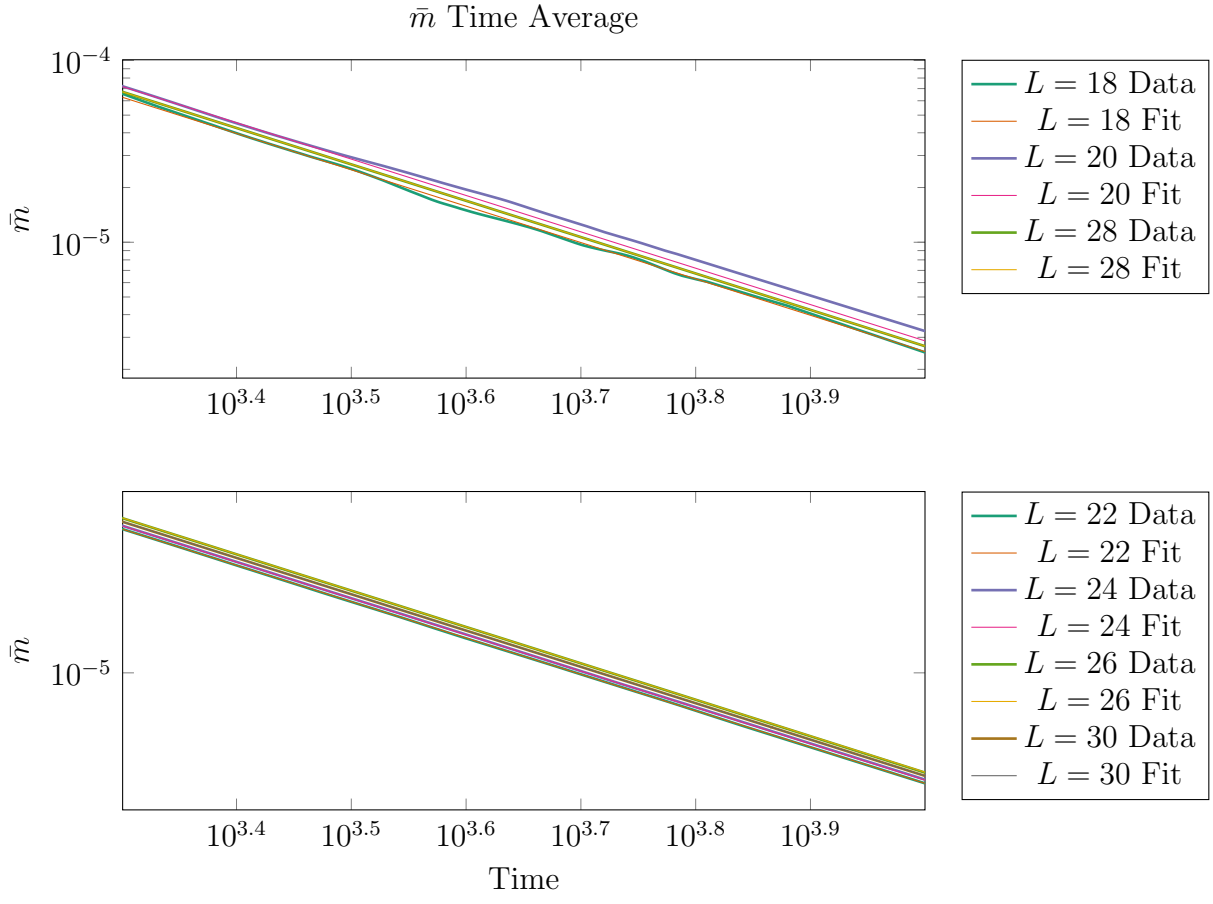

Figure 4.19: Late-time time-averaged decays of $\bar{m}$ for the fully polarized state for $\lambda = 0.6$ with power-law fits

The overall amplitude of the late-time power-law tail is nevertheless expected to retain sensitivity to early-time relaxation processes, since the majority of relaxation

weight is accumulated in the early-time regime. Due to this, it should be possible to recover the same dependence of early-time regime decay time on system size from the amplitude of the late-time power-law tails.

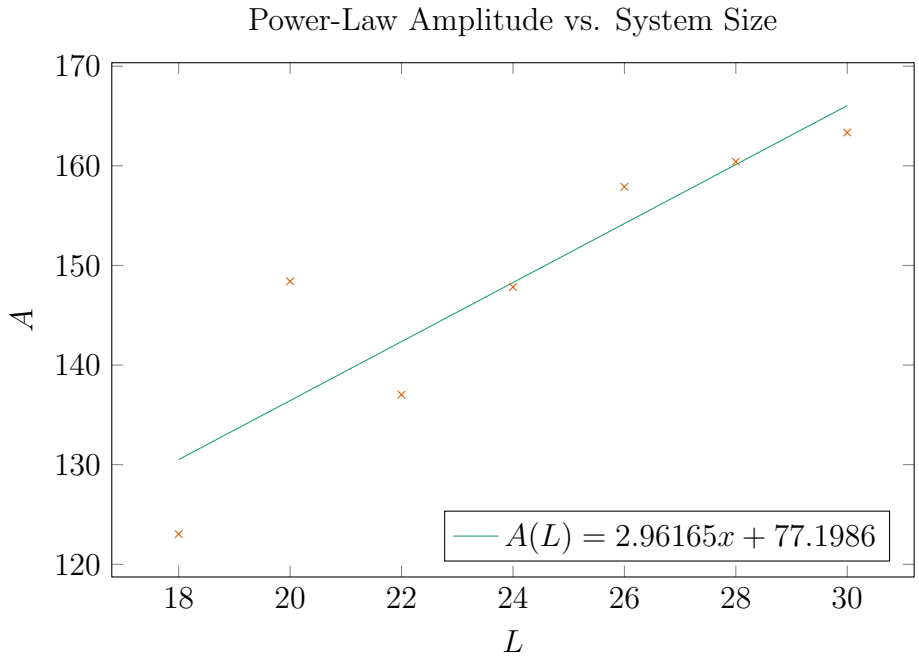

Figure 4.20: Extracted amplitudes A from the late-time power-law fits for $\bar{m}$ for the fully polarized state for $\lambda = 0.5$

The amplitudes do in fact recover the approximately linear relationship in the fully polarized state in Fig. 4.20. In Fig. 4.21 and Fig. 4.22, the amplitudes also recover the same relationship as the early-time regime fits. This lends more credence to the interpretation that early-time linear dependence is robust. In the dimer product state, the even-odd effect present in earlier extractions of the early-time regime decay times has disappeared in the amplitudes. This is expected, as late-time time-averaged relaxation is governed by increasingly averaged behavior, suppressing the even-odd effect.

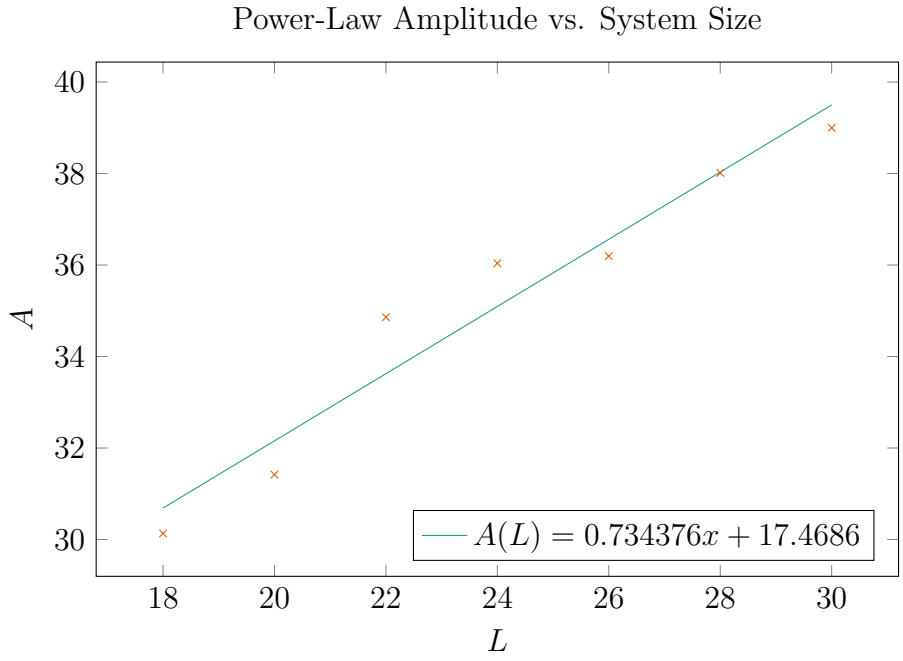

Figure 4.21: Extracted amplitudes A from the late-time power-law fits for σ_8^z for the Néel state for $\lambda = 0.5$

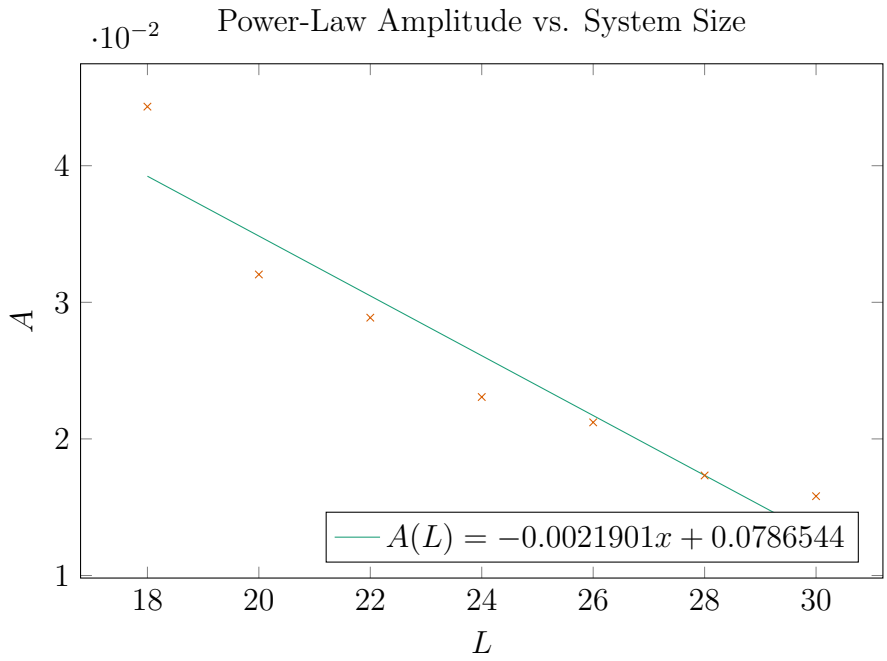

Figure 4.22: Extracted amplitudes A from the late-time power-law fits for $\sigma_8^z\sigma_9^z$ for the dimer product state for $\lambda = 0.5$

If the full decay was governed by a single relaxation process, the late-time power-

Initial State	λ	Observable	Late-Time Power Law
Fully Polarized	0.5	$\bar{m}$	t^{-2}
Néel	0.5	σ_8^z	t^{-2}
Néel	0.6	$\sigma_8^z\sigma_9^z$	t^{-2}
Dimer Product	0.5	σ_8^z	t^{-2}
Dimer Product	0.6	$\sigma_8^z\sigma_9^z$	$t^{-1.5}$

Figure 4.23: Comparison of the late-time power-law tail exponent for different observables and initial conditions

law would be expected to approach a simple $1/t$ decay. The observation that the non-trivial power-law decay is dependent on initial conditions indicates that the relaxation dynamics are not described by a single process. It naturally follows that the early-time regime probes local dephasing, while the late-time regime probes slower decay dynamics. The persistence of amplitude scaling, despite changes in the asymptotic power-law, suggests that the amplitude and exponents encode different physical properties.

The analysis of time-averaged observables in both the early-time regime and late-time regime has added evidence that the general qualitative trends seen in the early-time regime of raw decays are robust and not an artifact of fluctuations. The late-time approximate power-law tails also provide more evidence that the early-time and late-time regimes probe fundamentally different dynamics.

4.4.4 Plateau Fluctuations and Plateau Entry

4.4.4.1 Plateau Fluctuation Scaling

Once the system approaches the infinite-temperature regime, finite-size oscillations remain around the plateau value. These fluctuations are a direct consequence of finite-size effects of the accessible system sizes. Fig. 4.24 shows fluctuations around the plateau values for all system sizes centered at zero. The suppression of these oscillations with increasing system size is consistent across all studied states.

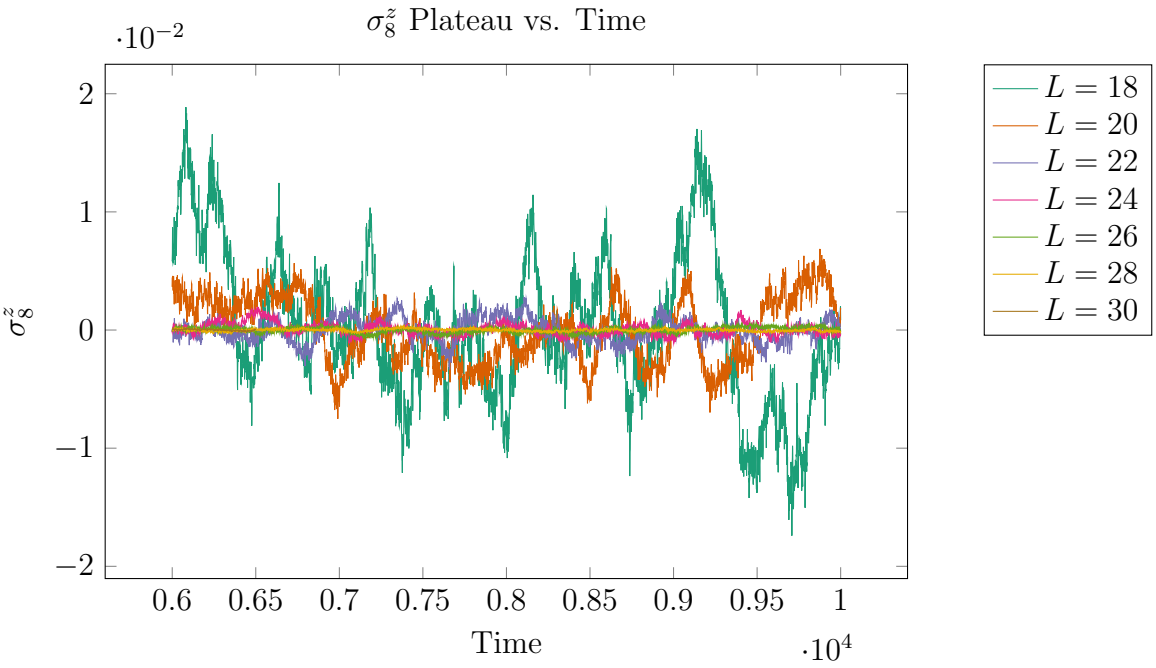

Figure 4.24: σ_8^z observable plateaus for fully polarized state for $\lambda = 0.5$

The fluctuation sizes are estimated by half the range of the plateau oscillations over a fixed late-time window. These fluctuations should be some function of system size, as they are explicitly not numerical noise but rather finite-size effects.

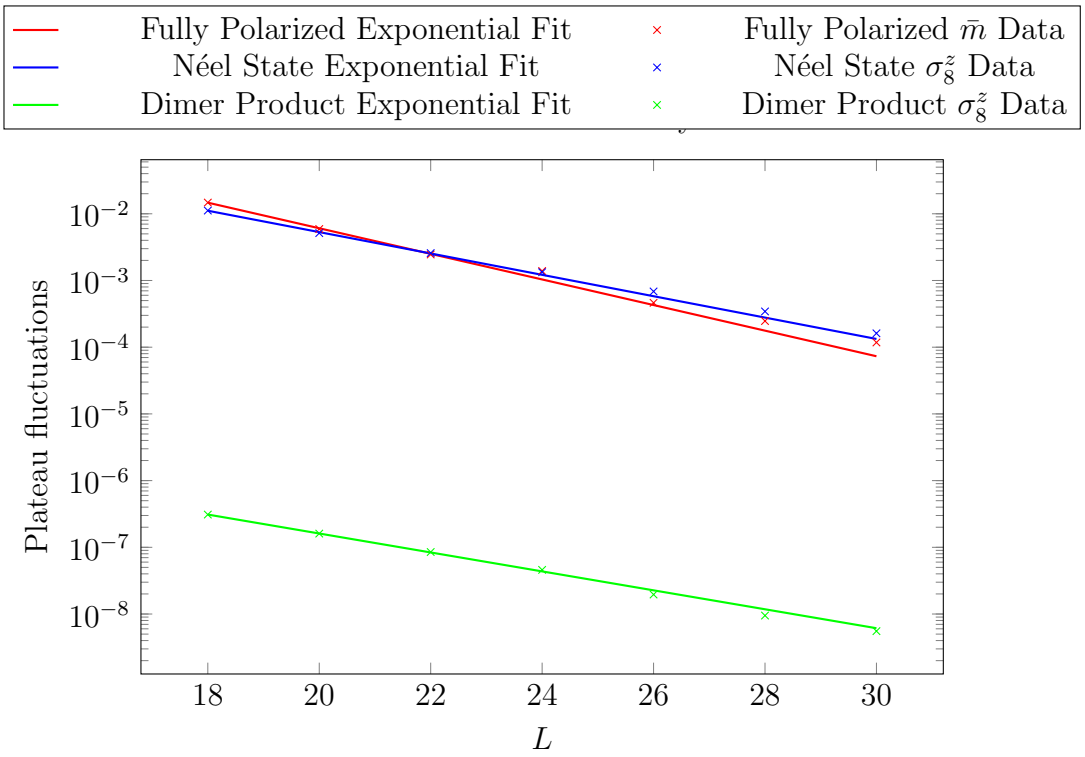

Figure 4.25: Plateau fluctuation size plotted against system size for all studied states

In all states, the finite-size fluctuations are strongly suppressed in system size. While there is not enough range to distinguish between exponential and power-law scaling, an exponential is motivated by ETH. Finite-size fluctuations of local observables in generic non-integrable systems have been found to scale as $D^{-1/2}$, where D is the Hilbert-space dimension [4]. For a spin chain, the Hilbert-space grows exponential with system size, $D \sim 2^L$. This corresponds to exponential suppression in L up to finite-size corrections, suggesting that plateau fluctuations probe residual finite-size fluctuations around the infinite-temperature limit.

4.4.4.2 plateau-entry times

Although the strength of the decays appear similar across system sizes, decays for larger systems continue much longer after the smaller system sizes start to plateau. This is due to the fact that not only are the plateau values larger for smaller systems, but so are the fluctuations around the plateau. This gives motivation for a new thermalization detection procedure. Instead of comparing the strength of the decays through fitting, thermalization time is defined as the point at which the observable becomes indistinguishable from a plateau oscillation.

To detect when the data has approached the plateau, plateau fluctuations are considered a statistical distribution to calculate the standard deviation. This is a more robust measure than the naive amplitude. Then, a thermalization time is defined for when the data approaches within $n\sigma$ of the infinite-temperature plateau value. The numerical data oscillates around the decay due to the inherited dynamics, which could produce artificially early plateau-entry times. To suppress the oscillatory dynamics, this window could be fitted with a stretched exponential to extract the decay time, or the data can be smoothed using a Gaussian filter. For the Néel and dimer product states, Gaussian smoothing produced more stable plateau-entry time estimates than direct fitting.

A stretched exponential provided significantly more stable fits over the full decay window than a standard exponential. A stretched exponential of the form

$$f(t) = A\exp[-t^C/B] + D \tag{4.11}$$

was used. Fig. 4.26 shows the stretched exponential fit for selected decays. The thermalization time can then be extracted from the fit by

$$t^* = \left(B\ln\left[\frac{|A|}{\sigma}\right]\right)^{1/C} \tag{4.12}$$

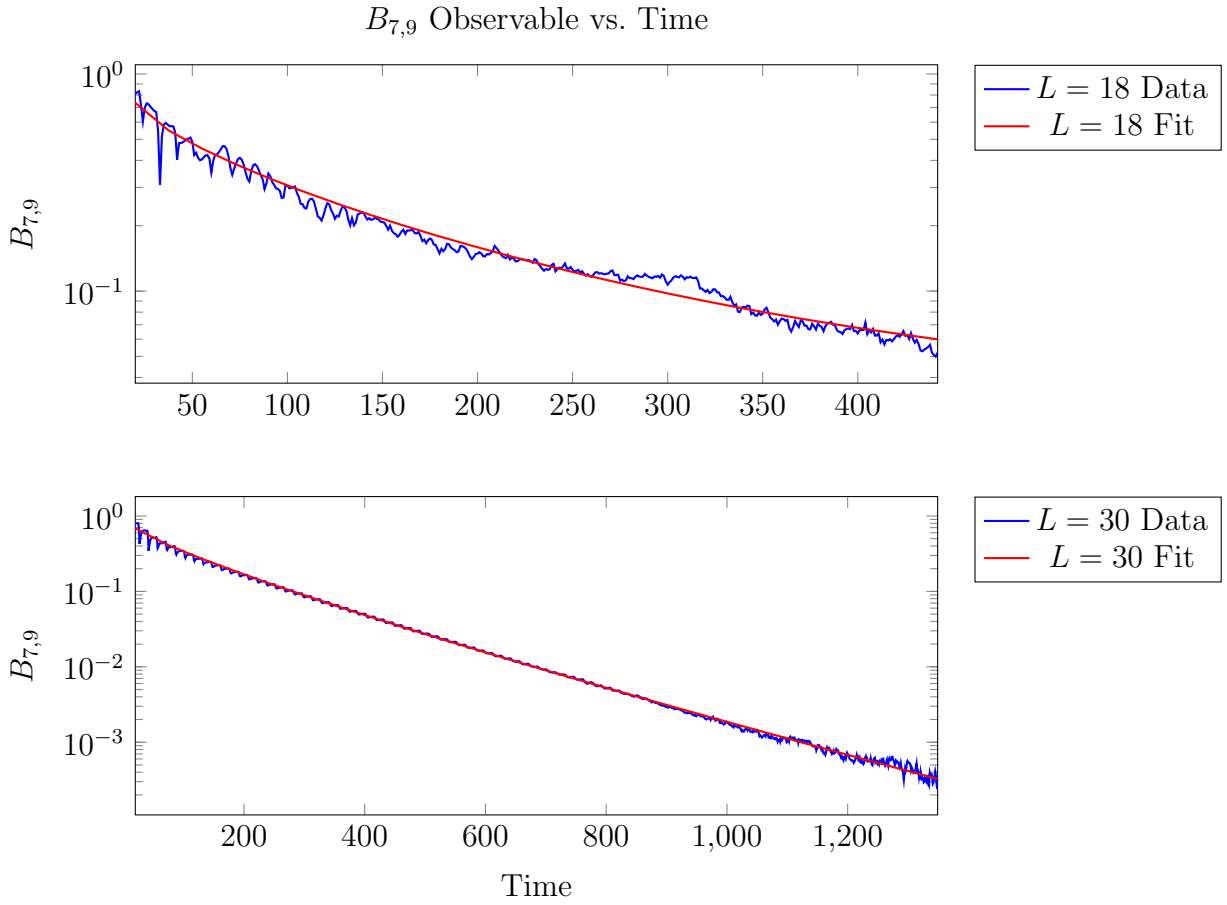

Figure 4.26: $B_{7,9}$ observable with a stretched exponential fit for the fully polarized state for $\lambda = 0.5$

Thermalization time can then be extracted from the fits. This is plotted with the inverse of extracted thermalization time against the inverse of system size. Plotting $1/t^*$ against $1/L$ incorporates the expectation that thermalization time will diverge in the thermodynamic limit. Therefore, including the origin as a data point constrains the fit to remain consistent with the expected thermodynamic-limit behavior. Fig. 4.27 shows that thermalization time scales quadratically with system size for the average magnetization. The bond strength term exhibits higher-order finite-size corrections, but accessible system sizes appear consistent with an approximately quadratic scaling regime in a crossover region due to some finite-size effects.

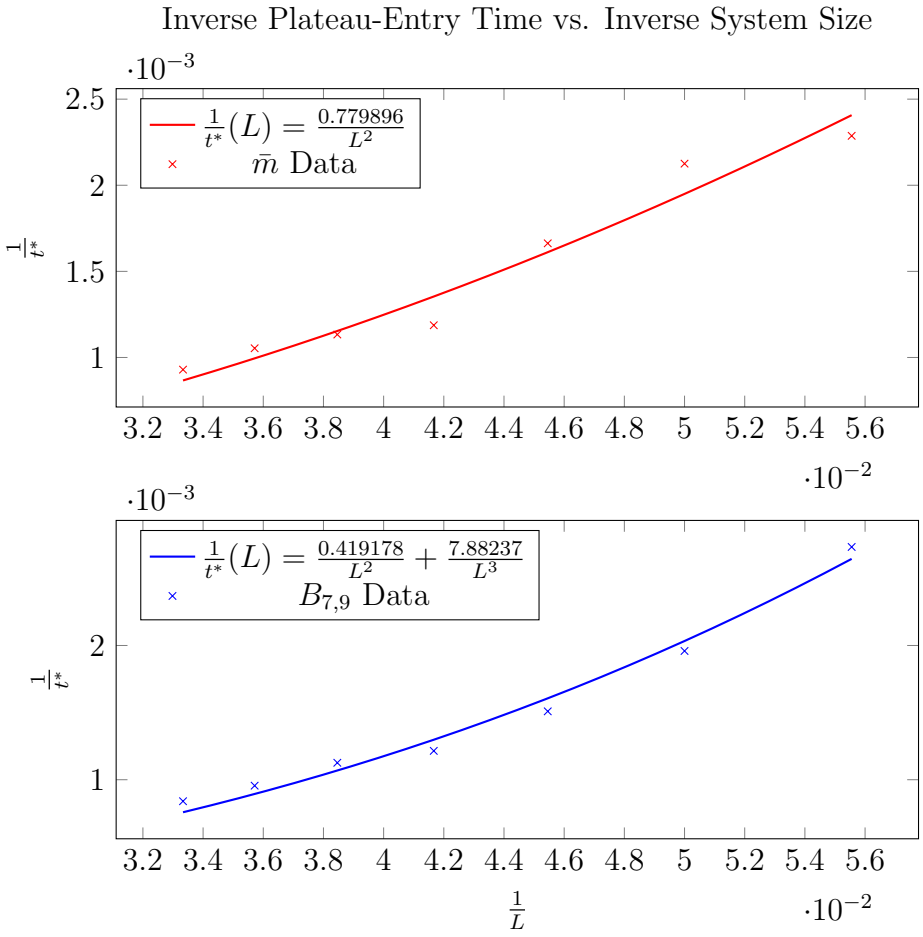

Figure 4.27: Plateau-entry time of $\bar{m}$ and $B_{7,9}$ for the fully polarized state for $\lambda = 0.5$

Instead of fitting decays in the Néel and dimer product states, thermalization time is extracted from when the smoothed data approaches within three standard deviations of the plateau value. Fig. 4.28 shows the raw decays of the $\sigma_8^z \sigma_9^z$ observable for $\lambda = 0.6$ where the decays are cutoff using this procedure. In this plot, there is a general monotonic trend where the cutoff activates. This is consistent with all observables tested.

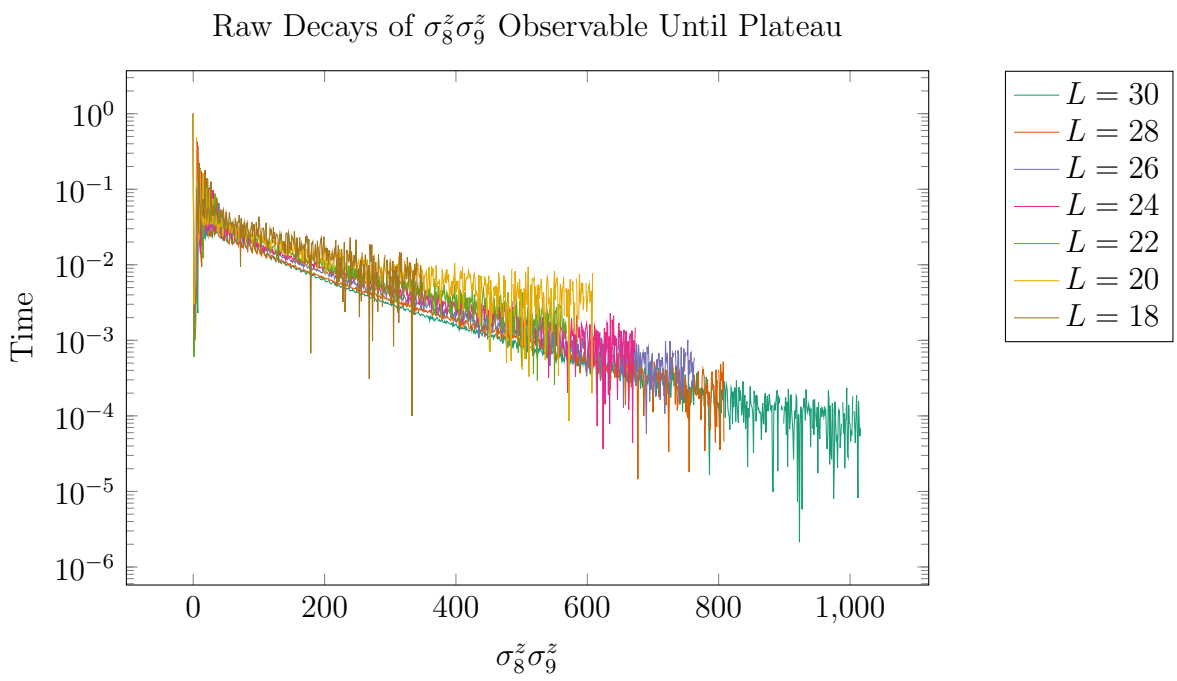

Figure 4.28: Cutoff regions for the $\sigma_8^z\sigma_9^z$ observables for the dimer product state for $\lambda = 0.6$

Inverting the axes again to enforce the thermodynamic limit, extracted thermalization times are plotted for the Néel state in Fig. 4.29 and for the dimer product state in Fig. 4.30. The extracted thermalization times are broadly consistent with quadratic scaling in system size in the thermodynamic limit. For single-site magnetization in the Néel state, the crossover region appears again, which could be due to the finite-size effects.

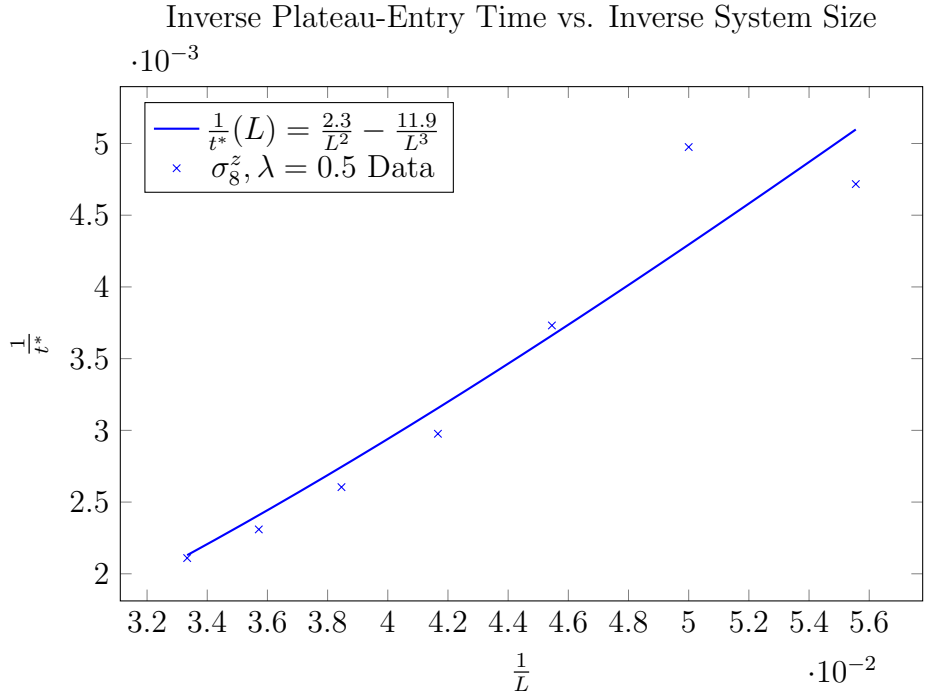

Figure 4.29: Plateau-entry time of σ_8^z for the Néel state for $\lambda = 0.5$

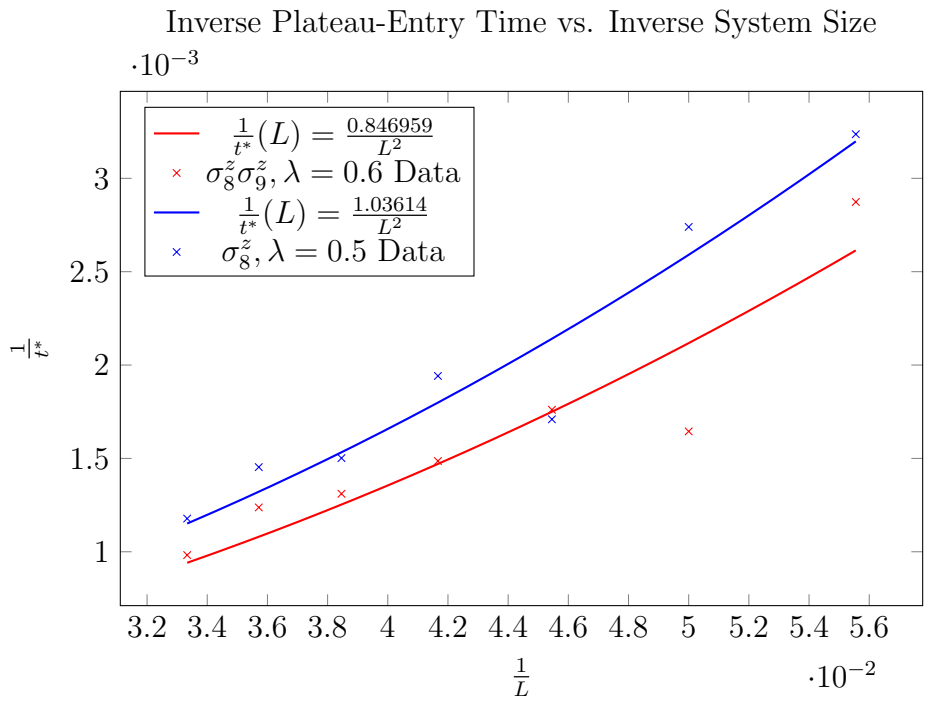

Figure 4.30: Plateau-entry time of σ_8^z and $\sigma_8^z\sigma_9^z$ for the dimer product state for $\lambda = 0.5, 0.6$

Using this procedure for extracting thermalization times can lead to a pronounced even-odd effect for some observables and initial states. For the $\sigma_8^z\sigma_9^z$ observable in the Néel state for both $\lambda = 0.6$ and $\lambda = 0.7$, there is an even-odd effect, where thermalization times for states satisfying $L \mod 4 = 2$ are approximately quadratic, and the states satisfying $L \mod 4 = 0$ exhibit a weaker scaling over the accessible sizes. The even-odd finite-size effects are not unexpected in a Floquet brickwork circuit, since the circuit is translationally invariant by two sites. This difference in apparent scaling suggests that finite-size effects in accessible systems depend on system parity.

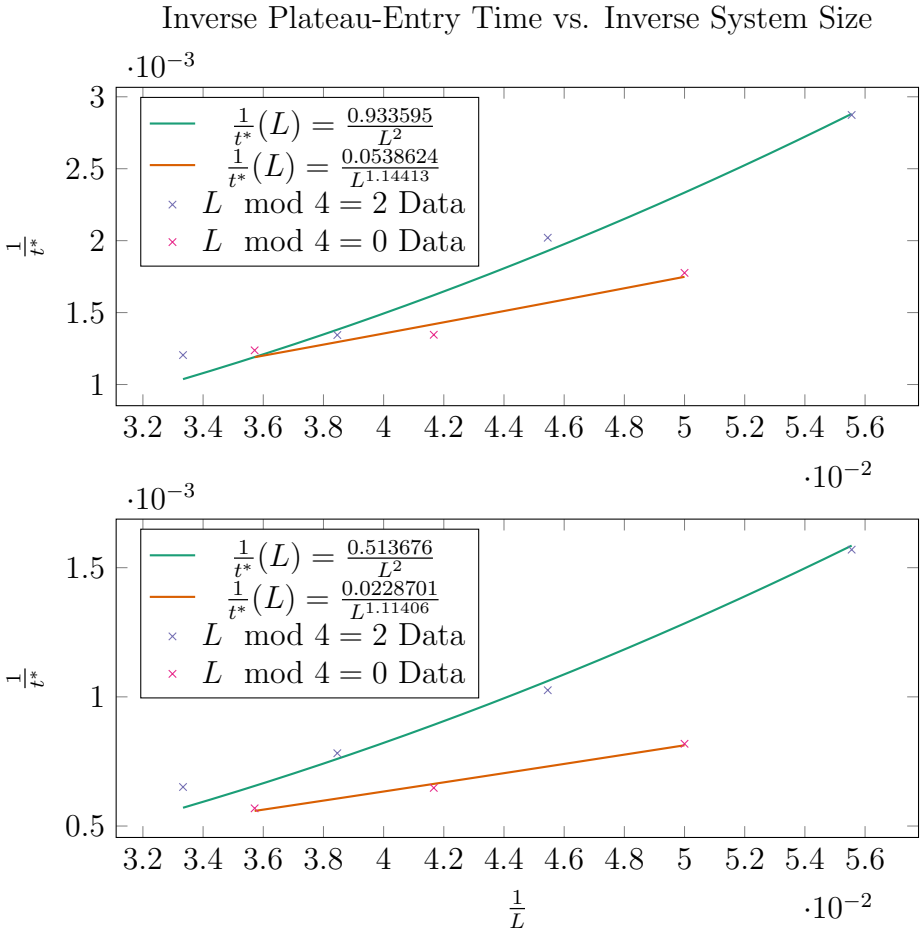

Figure 4.31: Even-odd effects of $\sigma_8^z\sigma_9^z$ for the Néel state for $\lambda = 0.6, 0.7$

Using plateau-entry time as thermalization time suggests that thermalization time could scale quadratically with system size. Different extraction procedures were used depending on the stability of the observable dynamics, although the resulting scaling behavior remained qualitatively consistent. In some initial states and observables,

significant even-odd effects appear with apparent dependence on $L \mod 4$, thereby changing the approximate scaling of thermalization time with system size. The accessible system sizes were insufficient to determine whether these trends converge in the thermodynamic limit; however, the discrepancy between the approximately linear early-time dephasing timescales and the approximately quadratic plateau-entry times suggests that local relaxation and global equilibrium occur on parametrically different timescales.

Chapter 5

Summary and Conclusions

In this thesis, we investigated the effects of a single non-integrable impurity in an otherwise integrable one-dimensional Floquet XXZ quantum circuit. Integrable systems are characterized by an extensive number of conserved quantities that constrain dynamics and prevent thermalization. By breaking integrability in the Floquet XXZ circuit through the introduction of a localized impurity that breaks the Yang-Baxter structure of the XXZ circuit, we study how formerly conserved quantities are gradually destabilized and how thermalization emerges.

The numerical results demonstrate that even a single local defect is enough to destabilize the integrable regime at sufficiently late times. Across a variety of initial states, including the fully polarized state, the Néel state, and the dimer product state, local observables that were previously conserved in the integrable regime decayed to a near-zero plateau value consistent with infinite-temperature thermalization.

The key goal of this work was to characterize how thermalization time scales with system size. Several complementary diagnostics were studied, including early-time exponential decay fits, time-averaged observables, and plateau-entry times. These results suggest that different diagnostics probe distinct relaxation processes. Early-time exponential fits exhibited approximately linear scaling with system size for several observables and remained robust under time averaging, suggesting early-time dynamics mainly probe local dephasing dynamics. In contrast, the plateau-entry times imply that thermalization could scale quadratically with system size in the thermodynamic limit. The difference between early-time decay fits and plateau-entry diagnostics suggests that impurity-induced relaxation may involve multiple dynamical regimes, with the late-time regime potentially reflecting hydrodynamic relaxation [15].

The plateau-entry diagnostic revealed finite-size effects beyond the approximately quadratic scaling seen in several observables. In particular, some observables in the Néel state exhibited pronounced even-odd effects depending on the parity of the system. Systems of size $L \mod 4 = 2$ exhibited approximately quadratic behavior, whereas systems satisfying $L \mod 4 = 0$ remained deep in an apparent crossover regime over the accessible system sizes. While similar crossover behavior was seen in the fully polarized state and the dimer product state, the substantial even-odd effect was not observed. This suggests that the plateau-entry procedure is sensitive to residual finite-size effects, and while plateau-entry times are broadly consistent with approximately quadratic scaling, accessible system sizes remain insufficient to definitively determine the asymptotic behavior.

The late-time time-averaged dynamics revealed evidence for nontrivial long-time relaxation behavior beyond the approximately exponential decay observed in the

early-time regime. The late-time regime of the time-averaged observables was approximately described by power-law tails whose exponents depended on the initial state, observable, and error parameter. Although the extracted exponents varied, early-time decay scales were recovered through the amplitudes. This implies that the amplitudes remain sensitive to local relaxation processes governing the initial decay, supporting the interpretation that the early-time regime probes primarily local dephasing, while the late-time regime probes slower relaxation processes. The nontrivial power-law tails, rather than the simple $1/t$ behavior expected from time-averaging a single exponential, implies that full relaxation dynamics are not described by a single process and instead involve multiple competing relaxation dynamics.

Finite-size plateau fluctuations provided additional evidence consistent with the Eigenstate Thermalization Hypothesis. The observed suppression of fluctuation amplitudes with increasing system size was qualitatively consistent with the expectation that off-diagonal elements of local observables in the energy eigenbasis are exponentially suppressed in system size.

This project also demonstrated the power of CUDA and GPU-accelerated parallelization for studying brickwork Floquet circuits. By exploiting the specific structure of the brickwork circuit, it was possible to design an embarrassingly parallel algorithm to simulate the behavior of the circuit. It was possible to simulate systems of up to 30 spins on consumer-grade laptops. These methods allowed for the study of long term dynamics that would be inaccessible using dense matrix methods.

There remains several important directions for future work. Access to larger system sizes would help distinguish true trends from finite-size effects and clarify the relationship between local dephasing and global thermalization timescales. It would also be of interest to investigate multiple impurities or different classes of Floquet circuits to determine how universal the observed behavior is.

Overall, this work highlights the fragility of integrability and the complexity of thermalization dynamics in Floquet quantum systems. Even a single localized defect can eventually drive the system to thermalize completely, but the resulting relaxation dynamics exhibit distinct timescales. Understanding the interplay between local dephasing, global thermalization, and integrability breaking remains an important open problem in non-equilibrium many-body quantum mechanics.

Bibliography

[1] Dmitry A. Abanin, Wojciech De Roeck, Wen Wei Ho, and François Huveneers. Effective hamiltonians, prethermalization, and slow energy absorption in periodically driven many-body systems. *Physical Review B*, 95(1), January 2017.

[2] R. J. Baxter. *Exactly Solved Models in Statistical Mechanics*, pages 5–63.

[3] Bruno Bertini, Pavel Kos, and Tomaž Prosen. Entanglement spreading in a minimal model of maximal many-body quantum chaos. *Physical Review X*, 9(2), May 2019.

[4] W. Beugeling, R. Moessner, and Masudul Haque. Finite-size scaling of eigenstate thermalization. *Phys. Rev. E*, 89:042112, Apr 2014.

[5] Marin Bukov, Luca D'Alessio, and Anatoli Polkovnikov. Universal high-frequency behavior of periodically driven systems: from dynamical stabilization to floquet engineering. *Advances in Physics*, 64(2):139–226, March 2015.

[6] Pasquale Calabrese and John Cardy. Time dependence of correlation functions following a quantum quench. *Physical Review Letters*, 96(13), April 2006.

[7] Amos Chan, Andrea De Luca, and J. T. Chalker. Solution of a minimal model for many-body quantum chaos. *Phys. Rev. X*, 8:041019, Nov 2018.

[8] A J Daley, C Kollath, U Schollwöck, and G Vidal. Time-dependent density-matrix renormalization-group using adaptive effective hilbert spaces. *Journal of Statistical Mechanics: Theory and Experiment*, 2004(04):P04005, April 2004.

[9] J. M. Deutsch. Quantum statistical mechanics in a closed system. *Phys. Rev. A*, 43:2046–2049, Feb 1991.

[10] Luca D'Alessio, Yariv Kafri, Anatoli Polkovnikov, and Marcos Rigol. From quantum chaos and eigenstate thermalization to statistical mechanics and thermodynamics. *Advances in Physics*, 65(3):239–362, May 2016.

[11] André Eckardt. Colloquium: Atomic quantum gases in periodically driven optical lattices. *Rev. Mod. Phys.*, 89:011004, Mar 2017.

[12] Fabian H. L. Essler. Quantum matter 3 lecture notes. `https://www-thphys.physics.ox.ac.uk/people/FabianEssler/QMat2/Qmat2.pdf`, 2025.

[13] Fabian H L Essler and Maurizio Fagotti. Quench dynamics and relaxation in isolated integrable quantum spin chains. *Journal of Statistical Mechanics: Theory and Experiment*, 2016(6):064002, 2016.

[14] L. D. Faddeev. How algebraic bethe ansatz works for integrable model, 1996.

[15] Aaron J. Friedman, Sarang Gopalakrishnan, and Romain Vasseur. Diffusive hydrodynamics from integrability breaking. *Physical Review B*, 101(18), May 2020.

[16] David Goldberg. What every computer scientist should know about floating-point arithmetic. *ACM Computing Surveys*, 23(1):5–48, 1991.

[17] Sarang Gopalakrishnan and Austen Lamacraft. Unitary circuits of finite depth and infinite width from quantum channels. *Phys. Rev. B*, 100:064309, Aug 2019.

[18] Gaël Guennebaud, Benoît Jacob, et al. Eigen. https://libeigen.gitlab.io, 2010.

[19] André Henriques. More about the yang-baxter equation. `http://andreghenriques.com/Seminars/SpinChainsTalk5.pdf`, 2014.

[20] Enej Ilievski, Marko Medenjak, Tomaž Prosen, and Lenart Zadnik. Quasilocal charges in integrable lattice systems. *Journal of Statistical Mechanics: Theory and Experiment*, 2016(6):064008, 2016.

[21] T Inami and H Konno. Integrable xyz spin chain with boundaries. *Journal of Physics A: Mathematical and General*, 27(24):L913–L918, December 1994.

[22] Hyungwon Kim, Tatsuhiko N. Ikeda, and David A. Huse. Testing whether all eigenstates obey the eigenstate thermalization hypothesis. *Physical Review E*, 90(5), November 2014.

[23] V. E. Korepin, A. G. Izergin, and N. M. Bogoliubov. Quantum inverse scattering method and correlation functions, 1993.

[24] Achilleas Lazarides, Arnab Das, and Roderich Moessner. Fate of many-body localization under periodic driving. *Physical Review Letters*, 115(3), 2015.

[25] Elliott H. Lieb and Derek W. Robinson. The finite group velocity of quantum spin systems. *Communications in Mathematical Physics*, 28(3):251–257, Sep 1972.

[26] Anne Matthies, Nicolas Dannenfeld, Silvia Pappalardi, and Achim Rosch. Thermalization and hydrodynamic long-time tails in a floquet system, 2025.

[27] Adam Nahum, Jonathan Ruhman, Sagar Vijay, and Jeongwan Haah. Quantum entanglement growth under random unitary dynamics. *Phys. Rev. X*, 7:031016, Jul 2017.

[28] Michael A. Nielsen and Isaac L. Chuang. *Quantum Computation and Quantum Information: 10th Anniversary Edition*. Cambridge University Press, 2010.

[29] NVIDIA. Cuda c++ programming guide. `https://docs.nvidia.com/cuda/`, 2024.

[30] NVIDIA Corporation. Cuda c++ best practices guide. `https://docs.nvidia.com/cuda/cuda-c-best-practices-guide/`, 2024. Accessed: 2026-05-22.

[31] Román Orús. A practical introduction to tensor networks: Matrix product states and projected entangled pair states. *Annals of Physics*, 349:117–158, October 2014.

[32] D. Perez-Garcia, F. Verstraete, M. M. Wolf, and J. I. Cirac. Matrix product state representations, 2007.

[33] Pedro Ponte, Anushya Chandran, Z. Papić, and Dmitry A. Abanin. Periodically driven ergodic and many-body localized quantum systems. *Annals of Physics*, 353:196–204, February 2015.

[34] Marcos Rigol, Vanja Dunjko, and Maxim Olshanii. Thermalization and its mechanism for generic isolated quantum systems. *Nature*, 452(7189):854–858, April 2008.

[35] Marcos Rigol, Vanja Dunjko, Vladimir Yurovsky, and Maxim Olshanii. Relaxation in a completely integrable many-body quantum system: An ab initio study of the dynamics of the highly excited states of 1d lattice hard-core bosons. *Phys. Rev. Lett.*, 98:050405, Feb 2007.

[36] Ulrich Schollwöck. The density-matrix renormalization group in the age of matrix product states. *Annals of Physics*, 326(1):96–192, January 2011.

[37] Jon H. Shirley. Solution of the schrödinger equation with a hamiltonian periodic in time. *Phys. Rev.*, 138:B979–B987, May 1965.

[38] Mark Srednicki. Chaos and quantum thermalization. *Physical Review E*, 50(2):888–901, August 1994.

[39] Matthieu Vanicat, Lenart Zadnik, and Tomaž Prosen. Integrable trotterization: Local conservation laws and boundary driving. *Physical Review Letters*, 121(3), 2018.

[40] Guifré Vidal. Efficient simulation of one-dimensional quantum many-body systems. *Physical Review Letters*, 93(4), 2004.